



**EMORY**  
LIBRARIES &  
INFORMATION  
TECHNOLOGY

**OpenEmory**

## **Revealing the activation pathway for TMEM16A chloride channels from macroscopic currents and kinetic models**

Juan A. Contreras-Vite, *Universidad Autónoma de San Luis Potosí*  
Silvia Cruz-Rangel, *Universidad Autónoma de San Luis Potosí*  
José J. De Jesus-Perez, *Universidad Autónoma de San Luis Potosí*  
Iván A. Arechiga Figueroa, *Universidad Autónoma de San Luis Potosí*  
Aldo A. Rodríguez-Menchaca, *Universidad Autónoma de San Luis Potosí*  
Patricia Perez-Cornejo, *Universidad Autónoma de San Luis Potosí*  
[Harrison Hartzell Jr.](#), *Emory University*  
Jorge Arreola, *Universidad Autónoma de San Luis Potosí*

---

**Journal Title:** Pflügers Archiv European Journal of Physiology

**Volume:** Volume 468, Number 7

**Publisher:** Springer Verlag | 2016-07-01, Pages 1241-1257

**Type of Work:** Article | Post-print: After Peer Review

**Publisher DOI:** 10.1007/s00424-016-1830-9

**Permanent URL:** <https://pid.emory.edu/ark:/25593/s4nr2>

---

Final published version: <http://dx.doi.org/10.1007/s00424-016-1830-9>

### **Copyright information:**

© 2016, Springer-Verlag Berlin Heidelberg.

*Accessed October 24, 2019 2:10 AM EDT*



Published in final edited form as:

*Pflugers Arch.* 2016 July ; 468(7): 1241–1257. doi:10.1007/s00424-016-1830-9.

## REVEALING THE ACTIVATION PATHWAY FOR TMEM16A CHLORIDE CHANNELS FROM MACROSCOPIC CURRENTS AND KINETIC MODELS

Juan A. Contreras-Vite<sup>1</sup>, Silvia Cruz-Rangel<sup>1</sup>, José J. De Jesús-Pérez<sup>1</sup>, Iván A. Aréchiga Figueroa<sup>2</sup>, Aldo A. Rodríguez-Menchaca<sup>3</sup>, Patricia Pérez-Cornejo<sup>3</sup>, H. Criss Hartzell<sup>4</sup>, and Jorge Arreola<sup>1\*</sup>

<sup>1</sup>Physics Institute, Universidad Autónoma de San Luis Potosí, Ave. Dr. Manuel Nava #6, San Luis Potosí, SLP 78290 México

<sup>2</sup>CONACYT - Universidad Autónoma de San Luis Potosí School of Medicine, Ave. V. Carranza 2405, San Luis Potosí, SLP 78290 México

<sup>3</sup>Department of Physiology, Universidad Autónoma de San Luis Potosí School of Medicine, Ave. V. Carranza 2405, San Luis Potosí, SLP 78290 México

<sup>4</sup>Department of Cell Biology, Emory University School of Medicine, Atlanta GA 30322

### Abstract

TMEM16A (ANO1), the pore-forming subunit of calcium-activated chloride channels, regulates several physiological and pathophysiological processes such as smooth muscle contraction, cardiac and neuronal excitability, salivary secretion, tumour growth, and cancer progression. Gating of TMEM16A is complex because it involves the interplay between increases in intracellular calcium concentration ( $[Ca^{2+}]_i$ ), membrane depolarization, extracellular  $Cl^-$  or permeant anions, and intracellular protons. Our goal here was to understand how these variables regulate TMEM16A gating and to explain four observations. a) TMEM16A is activated by voltage in the absence of intracellular  $Ca^{2+}$ . b) The  $Cl^-$  conductance is decreased after reducing extracellular  $Cl^-$  concentration ( $[Cl^-]_o$ ). c)  $I_{Cl}$  is regulated by physiological concentrations of  $[Cl^-]_o$ . d) In cells dialyzed with  $0.2 \mu M [Ca^{2+}]_i$ ,  $Cl^-$  has a bimodal effect: at  $[Cl^-]_o < 30 \text{ mM}$  TMEM16A current activates with a monoexponential time course, but above  $30 \text{ mM}$   $[Cl^-]_o$   $I_{Cl}$  activation displays fast and slow kinetics. To explain the contribution of  $V_m$ ,  $Ca^{2+}$  and  $Cl^-$  to gating, we developed a 12-state Markov chain model. This model explains TMEM16A activation as a sequential, direct, and  $V_m$ -dependent binding of two  $Ca^{2+}$  ions coupled to a  $V_m$ -dependent binding of an external  $Cl^-$  ion, with  $V_m$ -dependent transitions between states. Our model predicts that extracellular  $Cl^-$  does not alter the apparent  $Ca^{2+}$  affinity of TMEM16A, which we corroborated experimentally. Rather, extracellular  $Cl^-$  acts by stabilizing the open configuration induced by  $Ca^{2+}$  and by contributing to the  $V_m$  dependence of activation.

\*Corresponding Author: Dr. Jorge Arreola, Physics Institute, Universidad Autónoma de San Luis Potosí, Avenida Dr. Manuel Nava #6, Zona Universitaria, San Luis Potosí, SLP 78290, México, Tel. 52(444)826 2363 ext 136, arreola@dec1.ifisica.uaslp.mx, Fax: 52(444)813-3874.

Juan A. Contreras-Vite and Silvia Cruz-Rangel contributed equally to this work

## Keywords

Chloride channel; kinetics; patch clamp; permeation; gating; mathematical modelling

## INTRODUCTION

Cl<sup>-</sup> movements through Ca<sup>2+</sup> activated chloride (Cl<sup>-</sup>) channels (CaCCs) play important roles in many cellular functions such as regulation of smooth muscle contraction, regulation of cardiac and neuronal excitability, salivary secretion, and tumour growth and progression in many types of cancer [13, 21, 29, 40]. TMEM16A (ANO1) and TMEM16B (ANO2) are the pore-forming subunits of CaCCs [6, 45, 50]. The gating mechanism of these channels is quite complex. Gating requires increases in intracellular calcium concentration ([Ca<sup>2+</sup>]<sub>i</sub>), but also involves membrane depolarization, extracellular Cl<sup>-</sup> or permeant anions, and intracellular protons. Ca<sup>2+</sup>-dependent activation is coupled to V<sub>m</sub> [27, 35, 49] and is regulated by intracellular protons that compete for Ca<sup>2+</sup> binding [1, 8]. When [Ca<sup>2+</sup>]<sub>i</sub> is in the range of 0.1 – 0.8 μM, channel gating is strongly V<sub>m</sub>-dependent, and the I–V<sub>m</sub> relationships show outward rectification. Such V<sub>m</sub>-dependence is lost when [Ca<sup>2+</sup>]<sub>i</sub> > 5 μM. Hence, the dose-response curve to [Ca<sup>2+</sup>]<sub>i</sub> displays weak V<sub>m</sub>-dependence [2, 49, 52]. This V<sub>m</sub>-dependence is explained by a voltage-dependent Ca<sup>2+</sup> dissociation [49]. We have shown that TMEM16A and TMEM16B exhibit fast and slow gating modes [11]. Both modes depend on intracellular Ca<sup>2+</sup>, membrane voltage (V<sub>m</sub>) and the extracellular Cl<sup>-</sup> concentration ([Cl<sup>-</sup>]<sub>o</sub>). Apart from the Ca<sup>2+</sup>-dependent activation, TMEM16A can also be activated by strong depolarizations in the absence of intracellular Ca<sup>2+</sup> [49].

We assume that direct binding of Ca<sup>2+</sup> activates TMEM16A [2, 3, 27]. This idea is supported by the following observations: a) injection of Ca<sup>2+</sup>, Ba<sup>2+</sup> or Sr<sup>2+</sup> into *Xenopus* oocytes activates CaCC [32]; b) TMEM16A in excised patches or liposomes can be activated by Ca<sup>2+</sup>, Ba<sup>2+</sup> or Sr<sup>2+</sup> [34, 46, 49]; c) mutating residues E702, E705, E730 and D734 located in the Ca<sup>2+</sup> binding pocket of TMEM16A decrease the Ca<sup>2+</sup> sensitivity 100 – 1000-fold [47, 52]; d) the x-ray structure of the *Nectria haematococca* TMEM16 homolog (*nh*TMEM16) shows the presence of two Ca<sup>2+</sup> ions bound to a site located within the membrane [5]; e) changing the *nh*TMEM16 Ca<sup>2+</sup>-coordinating residues significantly reduces the functional Ca<sup>2+</sup> sensitivity, which strongly indicates these residues are part of a high-affinity Ca<sup>2+</sup> binding site [5, 34, 47]; and f) vertebrate TMEM16A is activated in a cooperative manner by Ca<sup>2+</sup> [49]. Also, other regions of TMEM16A including the N-terminus and the first intracellular loop have been shown to contribute to Ca<sup>2+</sup> sensitivity [17, 49]. Thus, the existing evidence strongly suggests that TMEM16A is directly activated by binding at least two Ca<sup>2+</sup> ions.

The role of permeant ions in channel gating has increasingly been recognized. Gating of Cl<sup>-</sup> channels such as CIC-2, volume-sensitive channels, and CFTR are reported to be dependent on permeant anion [23, 25, 41, 51]. CaCCs are not the exception. Anions with a higher permeability than Cl<sup>-</sup> such as SCN<sup>-</sup>, I<sup>-</sup>, and NO<sub>3</sub><sup>-</sup> when applied from the extracellular side promote opening and accelerate the opening rate while slowing down the closing rate in CaCCs [4, 36, 38, 49]. In addition, these anions decrease the EC<sub>50</sub> for Ca<sup>2+</sup> both in *Xenopus*

oocyte CaCCs as well as heterologous-expressed TMEM16A and TMEM16B [4, 38, 39]. These observations suggest gating and ion permeation are coupled in TMEM16A channels.

The rather complex gating of TMEM16 channels cannot be understood without the help of a model. In this work, we developed a 12-state Markov chain model to explain the TMEM16A gating mechanism. The model reproduces the complex TMEM16A activation in response to  $V_m$ ,  $Ca^{2+}$  and different  $[Cl^-]_o$ . The model also predicts that extracellular  $Cl^-$  does not alter the channel's affinity for  $Ca^{2+}$ . Further experiments corroborated this prediction. We propose that TMEM16A is activated by sequential, direct,  $V_m$ -dependent binding of two  $Ca^{2+}$  ions coupled by a  $V_m$ -dependent binding of one external  $Cl^-$  ion.

## MATERIALS AND METHODS

### Culture of HEK 293 cells and expression of TMEM16A

Human embryonic kidney 293 cells (HEK293) were cultured in Dulbecco's modified Eagle medium (DMEM, Gibco BRL, Carlsbad, CA, USA) supplemented with 10% heat-inactivated fetal bovine serum, 1% gentamicin and 1% L-glutamine at 37 °C in a 95%  $O_2$ /5%  $CO_2$  atmosphere. Stable cell lines were developed by transfecting a cDNA encoding the mouse TMEM16A (ac variant) sub-cloned into the bi-cistronic expression vector pIRES2-EGFP (Clontech, Mountain View, CA, USA.). The PolyFect transfection reagent (Qiagen, Valencia, CA, USA) was used according to the manufacturer's specification. After 24 h, the cells were transferred to 24-well plates at low density in DMEM medium supplemented with 1 mg/ml G418 (Sigma- Aldrich Co. St. Louis, MO, USA.). G418-resistant transformants were identified by EGFP fluorescence and expanded. Stable cell lines were maintained in medium supplemented with G418 at 500  $\mu$ g/ml. Cells were seeded at low density on 5 mm circular coverslips before electrophysiological recordings.

### Recording solutions

Table 1 lists the composition of external solutions (ES) and internal solutions (IS) used to record the  $Cl^-$  current activated by intracellular  $Ca^{2+}$  or  $V_m$  ( $I_{Cl}$ ). IS with buffered  $Ca^{2+}$  was prepared using EGTA and  $Ca^{2+}$ ; the free  $[Ca^{2+}]_i$  was estimated using MAXCHELATOR ([maxchelator.stanford.edu](http://maxchelator.stanford.edu)). ES-140Cl and IS-40Cl/0.2Ca are control solutions. An IS with 5  $\mu$ M  $[Ca^{2+}]_i$  (IS-40Cl/5Ca) was used to activate fully TMEM16A and record  $I_{Cl}$  with long depolarizations in cells bathed with ES-140Cl. To analyse the activation of TMEM16A in zero  $[Ca^{2+}]_i$  we used IS-40Cl/0Ca containing 25.2 mM EGTA and 50 mM HEPES. The  $Cl^-$  dependence of activation was studied using ES containing 140, 109, 70.5, 30, 10 or 1.5 mM  $[Cl^-]_o$ . The pH of each solution was adjusted to 7.3 with TEA-OH or NaOH. ES was made hypertonic relative to the internal solutions to avoid activation of volume-sensitive  $Cl^-$  channels present in HEK293 cells [23]. Osmolarity was adjusted by adding D-mannitol and measured using the vapour pressure point method (VAPRO, Wescor Inc., South Logan, UT, USA). All chemicals were purchased from Sigma-Aldrich (Co. St. Louis, MO, USA.).

### Electrophysiological recordings

We record  $I_{Cl}$  at room temperature using the whole cell configuration of the patch clamp technique. Cells were held at  $-60$  mV and the  $V_m$  was changed stepwise from  $-100$  mV to

+160 mV or +180 mV in 20 mV increments, and then returned to -60 mV or -100 mV. Pulse duration varied between 0.5 to 20 s.  $I_{Cl}$  was recorded with an Axopatch 200B amplifier (Molecular Devices, Sunnyvale, CA, USA); currents were filtered at 5 kHz and digitized at 10 kHz for 0.5 s pulses. For 20 s pulses, the currents were filtered at 1 kHz and digitized at 2 kHz using pClamp software. Errors due to liquid junction potentials (-4.8 to -6.6 mV for our recording solutions) were minimized by using a 0.5 M KCl agar-bridge to ground the recording chamber and not corrected.

The effects of  $[Cl^-]_o$  on TMEM16A activation were determined by measuring the magnitude of tail currents ( $I_{tail}$ ) at -100 mV after a depolarising test pulse to +120 mV whose duration was varied from 0 to 3 s. The initial magnitude of  $I_{tail}$  after each pulse and each  $[Cl^-]_o$  was used to calculate the tail conductance ( $G_{tail}$ ) as a function of time and  $[Cl^-]_o$  using Equation 1.

$$G_{tail} = \frac{I_{tail}}{V_m - V_{rev}} \quad \text{Equation 1}$$

where  $V_{rev}$  is the reversal potential of  $I_{Cl}$ .  $G(t, [Cl^-]_o)$  was then normalized to the conductance obtained at the end of a 3 s test pulse with 140 mM  $Cl^-$ . The resulting normalized  $G$  vs time curve represented the time course of TMEM16A activation at +120 mV at each  $[Cl^-]_o$ . Dose-response curves were constructed using recordings obtained from patches excised from cells stably expressing TMEM16A. Patches were held at the desired  $V_m$  and exposed to increasing  $[Ca^{2+}]_i$  ranging from 0 to 12  $\mu$ M (Table 1) using a Fast-Step Perfusion System (VC-77SP Warner Instruments, Hamden, CT, USA). In between each  $[Ca^{2+}]_i$  test solution, a control solution containing 0  $Ca^{2+}$  and 25.2 mM EGTA was applied to check for changes in seal resistance.  $I_{Cl}$  was recorded with an Axopatch 200B amplifier, filtered at 1 kHz and digitized at 10 kHz.

### Analysis and modelling

The magnitude of  $I_{Cl}$  at each  $V_m$  was converted to conductance using Equation 1. Normalization was carried out using either  $G_{+120mV}$  or  $G_{max}$  to obtain  $G_{Norm}$  ( $G/G_{max}$  or  $G/G_{+120mV}$ ), which is proportional to the apparent open probability of the channel. We extracted the time constants by fitting the data to a mono or bi-exponential function of the form:

$$y_0 + a^{-t/\tau} \quad \text{or} \quad y_0 + a^{-t/\tau_f} + b^{-t/\tau_s} \quad \text{Equation 2}$$

where  $y_0$  is the value of  $y$  when  $t \rightarrow \infty$ ,  $t$  is the time,  $\tau$  is a time constant,  $a$  and  $b$  are the contribution of fast and slow processes, and  $\tau_f$  and  $\tau_s$  are the fast and slow time constants [11], respectively. The dose-response curves were constructed using normalized currents; only patches with stable basal current obtained with 0  $[Ca^{2+}]_i$  were used. In each case the basal current was subtracted to obtain the magnitude of the current activated by a given  $[Ca^{2+}]_i$ . The currents obtained from a particular patch were normalized to the maximum current estimated using equation:

$$\frac{I_{Cl}}{I_{max}} = \left[ \frac{1}{1 + \frac{EC_{50}}{[Ca^{2+}]_i}} \right]^{n_H} \quad \text{Equation 3}$$

where  $I_{max}$  is the estimated maximum current,  $EC_{50}$  is the  $[Ca^{2+}]_i$  needed to obtain  $I_{max}=0.5$ , and  $n_H$  is the Hill coefficient. To search for a kinetic scheme able to describe the time- and  $V_m$ -dependencies of  $I_{Cl}$  collected under a variety of experimental conditions we used Markov chain kinetic models [9] because they provide a good description of gating properties for different channels [24, 26, 28, 43, 48]. Different models with various discrete closed (C) and open (O) states were built using IChMASCOT software [10, 42]. Experimental and model  $I_{Cl}$  vs  $V_m$ ,  $G_{Norm}$  vs  $[Ca^{2+}]_i$ , and  $EC_{50}$  were compared. Finally, by computing the probability of occupation of each of the kinetic states as a function of time we aimed to find the activation route(s) of TMEM16A. In the model, a given transition was controlled by forward and backward rate constants, which were  $V_m$ -dependent in most cases:

$$k_f = k_{f,0} * e^{\frac{z_f F V_m}{RT}} \quad \text{and} \quad k_r = k_{r,0} * e^{-\frac{z_r F V_m}{RT}} \quad \text{Equation 4}$$

where  $k_f$  and  $k_r$  are forward and backward rate constants, respectively,  $k_{f,0}$  and  $k_{r,0}$  are the values of  $k_f$  and  $k_r$  at  $V_m=0$ ,  $z_f$ ,  $z_r$  are the apparent gating charges associated with a given transition,  $F$  is the Faraday constant,  $R$  is gas constant, and  $T$  is the temperature. The most likely values of the rate constant parameters at  $V_m = 0$  mV for a given model were obtained by best-fits as described in [12]. For that purpose, the squared differences between experimental and modelled values were minimized as follows:

$$\sum_{i=1}^N W_i \sum_{j=1}^{M_i} (E_{ij} - S_{ij})^2 \quad \text{Equation 5}$$

and

$$W_i = \frac{w_i}{M_i W E_{imax}^2} \quad \text{Equation 6}$$

where  $N$  = number of different data sets included in the global fitting procedure;  $M_i$  = number of independent experimental observations in the dataset  $i$ ;  $E_{ij}$  = experimental values of a given observation,  $S_{ij}$  = modelled values of a given observation;  $W_i$  = normalized weight factor for specific dataset;  $w_i$  = arbitrary weight factor for the measurement  $i$ ; and  $E_{imax}$  = maximal experimental value for the dataset  $i$ . The global fit was repeated 15 times. The resulting values were averaged and then used for the final fit to obtain the values reported in Table 2. Subsequently, we simulated the steady-state activation properties of TMEM16A using the IonChannelLab software [44] along with the rate constants previously determined with IChMASCOT. The experimental conditions to be tested such as  $[Ca^{2+}]_i$ ,

$[Cl^-]_o$ ,  $[Cl^-]_i$ , and  $V_m$  were included. To determine the most likely activation pathway, we calculated the probability (P) that TMEM16A stayed in a given state of a chosen gating kinetic model. For that purpose, the differential equations describing the time dependence of P (Equations 1 – 12 in Supplemental material) were numerically integrated using the Gear's BDF method. P was calculated for 20 s depolarizations with 0.2  $\mu M$   $[Ca^{2+}]_i$ , 140 mM and 30 mM  $[Cl^-]_o$  and 40 mM  $[Cl^-]_i$  and for 1 s depolarizations with 0  $\mu M$   $[Ca^{2+}]_i$ , 140 mM and 30 mM  $[Cl^-]_o$  and 40 mM  $[Cl^-]_i$  using the rate constants listed in Table 2.

Figures and fits were constructed using Origin (Origin Lab, Northampton, MA). Data were plotted as mean  $\pm$  SEM of n (number of independent experiments). Dashed black lines and arrows in each Figure indicate  $I_{Cl}=0$ . Where necessary, a Student t-test was used to evaluate statistically significant differences between data sets at  $P<0.05$ ; as indicated by the \* symbol.

## RESULTS

Here we characterized the effects of  $V_m$  and  $[Cl^-]_o$  on TMEM16A gating. We used these data to build a kinetic model to explain the contribution of  $V_m$ ,  $Ca^{2+}$ , and  $Cl^-$  to TMEM16A gating. Finally, using the model we predict the most likely pathway taken by the channel during activation.

### Activation of TMEM16A in the absence of intracellular $Ca^{2+}$

Under physiological conditions, CaCCs are activated by depolarization and increases in  $[Ca^{2+}]_i$  [2, 27, 31, 35]. However, TMEM16A can be activated even when no  $Ca^{2+}$  is present on the cytosolic side [49]. Here we recorded whole cell  $Cl^-$  currents ( $I_{Cl}$ ) in the absence of intracellular  $Ca^{2+}$  (with 25.2 mM EGTA).  $I_{Cl}$  displays fast onset kinetics and lacks an inward tail ( $I_{tail}$ ) current upon repolarization to  $-100$  mV (Figure 1A, black traces). The current is inhibited with 100  $\mu M$  tannic acid, a TMEM16A blocker (Figure 1A, bottom panel). To strengthen the assertion that the current was carried through TMEM16A in the absence of intracellular  $Ca^{2+}$ , we replaced external  $Cl^-$  with  $SCN^-$ , a more permeable anion that accelerates opening and retards channel closing [36, 49]. Figure 1B shows representative current traces recorded at  $+160$  mV from a cell bathed first with 140 mM  $Cl^-$  then 140 mM  $SCN^-$ . This manoeuvre increased the current (Figures 1B and 1C, triangles), consistent with  $SCN^-$  permeating through TMEM16A. However, we could not determine a definite reversal potential of the current in zero  $[Ca^{2+}]_i$  to calculate the permeability ratio  $P_{SCN}/P_{Cl}$ . In contrast,  $I_{Cl}$  was negligible at every  $V_m$  in cells transfected with an empty vector (Figure 1D). These results indicate that the  $I_{Cl}$  recorded in zero  $Ca^{2+}$  is flowing through TMEM16A activated by  $V_m$  and not through some other endogenous conductance.

### $Cl^-$ -dependence of TMEM16A gating

To analyse the effect of extracellular  $Cl^-$  we recorded  $I_{Cl}$  at different  $[Cl^-]_o$ . Figure 2A shows examples of  $I_{Cl}$  recorded from the same cell dialyzed with an IS containing 0.2  $\mu M$   $[Ca^{2+}]_i$ , 40 mM  $[Cl^-]_i$ , that was sequentially exposed to 140 mM, 70 mM and 10 mM  $[Cl^-]_o$ . The  $I_{Cl}$  magnitude decreased when  $[Cl^-]_o$  was reduced. This is summarized in the  $I_{Cl}$  vs  $V_m$  curves in Figure 2B. Since reduction of  $[Cl^-]_o$  from 140 mM to 10 mM increased the driving

force ( $V_m - V_{rev}$ ) from  $-92.6 \pm 2.5$  mV to  $-146.2 \pm 4.6$  mV, we expected a 1.6-fold increase in  $I_{tail}$  amplitude at  $-100$  mV. However,  $I_{tail}$  in 10 mM  $Cl^-$  did not increase; instead it fell drastically; the mean  $I_{tail\_10mM}/I_{tail\_140mM}$  ratio was  $0.78 \pm 0.05$  ( $n=7$ ). The time constant values of  $I_{tail}$  at  $-100$  mV after the pre-pulse to  $+160$  mV were  $47 \pm 4$  ms and  $43.7 \pm 3.1$  ms with 140 mM and 10 mM  $[Cl^-]_o$ , respectively, indicating no change in kinetics. When the conductance was calculated using the current magnitude at the end of each pulse and normalized using the value at  $+120$  mV ( $G_{Norm}$ ), we observed a 5-fold conductance drop at each  $V_m$  (Figure 2C) when  $[Cl^-]_o$  was reduced from 140 mM to 10 mM. Thus, at low external  $[Cl^-]_o$  the apparent open probability of TMEM16A declines.

To determine the effects of  $[Cl^-]_o$  on time-dependent activation we recorded  $I_{tail}$  from the same cell sequentially exposed to 140, 109, 70, 30, 10 and 1.5 mM. The cells were dialyzed with an IS containing  $0.2 \mu M Ca^{2+}$  and 40 mM  $Cl^-$ . Figure 3A shows representative recordings. Tail currents were obtained at  $-100$  mV after a  $+120$  mV depolarization as shown in the voltage protocol. In this case, we lengthened the depolarization from 0.5 s to 3 s in 0.5 s increments. At 140 mM  $[Cl^-]_o$  the  $I_{tail}$  amplitude (indicated by arrows) increased with longer pulses. In contrast, with 10 mM  $[Cl^-]_o$  the  $I_{tail}$  magnitude was smaller. This finding could be explained if gating is dependent on  $[Cl^-]_o$ . In Figure 3B,  $G_{Norm}$  at the indicated  $[Cl^-]_o$  is plotted as a function of pulse duration. The graph shows that decreasing the  $[Cl^-]_o$  from 140 mM to 10 mM produces a 3-fold reduction in  $G_{Norm}$ . A 5-fold decrease in  $G_{Norm}$  is observed when comparing 140 mM with 1.5 mM  $[Cl^-]_o$ . At  $[Cl^-]_o = 30$  mM,  $G_{Norm}$  levelled off and the  $G_{Norm}$  vs time curves were described by a single exponential function (solid lines) with  $\tau = 293.7 \pm 17$  ms and  $334 \pm 19.6$  ms for 1.5 mM and 10 mM  $[Cl^-]_o$ , respectively. However, with  $[Cl^-]_o > 30$  mM, only the initial part (time  $< 0.5$  s) of the curves was described by a single exponential because as pulse duration increased  $G_{Norm}$  rose in an almost linear fashion.  $\tau = 368.2 \pm 23$  ms and  $353.4 \pm 23.1$  ms for 109 mM and 140 mM  $[Cl^-]_o$ , respectively.

In cells bathed with a solution containing 140 mM or 30 mM  $[Cl^-]_o$  we extended the duration of the  $V_m$  pulses to 20 s and found that  $I_{Cl}$  displayed a second mode of gating, something we previously reported [11]. Figure 3C shows that the conductance was reduced nearly 22-fold upon switching from 140 mM to 30 mM  $[Cl^-]_o$  (note the scale bar is 10-times smaller for 30 mM  $[Cl^-]_o$ ). At 140 mM  $[Cl^-]_o$  (left) the  $G_{Norm}(t)$  at  $+140$  mV continuously increased for the entire 20 s pulse duration. The time course had a fast ( $\tau_f = 448.1 \pm 26.3$  ms) onset followed by a slower rise ( $\tau_s = 19.1 \pm 3.8$  s). The contributions of the fast and slow components were  $0.17 \pm 0.04$  and  $0.83 \pm 0.04$ , respectively. With 30 mM  $[Cl^-]_o$ ,  $G_{Norm}(t)$  was described by a  $\tau_f$  of  $368.6 \pm 55.5$  ms and  $\tau_s$  of  $6.2 \pm 1.5$  s; however, the fractional contribution of the fast and slow phases were reversed:  $0.92 \pm 0.1$  and  $0.08 \pm 0.1$ , respectively. These observations reinforce the conclusion that TMEM16A gating depends on  $[Cl^-]_o$ . We next asked if the  $Cl^-$  effect on gating would also occur in the presence of high  $[Ca^{2+}]_i$ , a condition that maximally activates TMEM16A [49]. To test this, we recorded  $I_{Cl}$  from cells dialyzed with  $5 \mu M [Ca^{2+}]_i$ . Figure 3D shows a trace obtained by averaging the current from 8 cells that were bathed in 140 mM  $[Cl^-]_o$  and depolarized to  $+100$  mV for 20 s and then repolarized to  $-60$  mV. Under these conditions,  $I_{Cl}$  did not display dual gating, instead the current had a monoexponential time course with  $\tau$  of  $3.7 \pm 0.36$  s. Taken



together, our data demonstrate that TMEM16A gating is dependent on external  $\text{Cl}^-$  but the  $\text{Cl}^-$  effects are attenuated when high  $[\text{Ca}^{2+}]_i$  activates the channel.

### Kinetic analysis of TMEM16A gating

The data in Figures 1, 2 and 3 as well as evidence cited in the Introduction highlight the complexity of TMEM16A activation. In an effort to have an integrated view of the activation mechanism we constructed a kinetic model that takes into account the  $V_m$ ,  $\text{Ca}^{2+}$ , and  $[\text{Cl}^-]_o$  dependencies of TMEM16A. Scheme IV in Figure 4 presents a 12-state model with 26 free parameters that satisfactorily reproduce the  $V_m$ ,  $\text{Ca}^{2+}$  and  $\text{Cl}^-$  dependencies of channel activation. The model was built based on the following experimental data and assumptions:

1. TMEM16A can be activated by  $V_m$  in the absence of intracellular  $\text{Ca}^{2+}$  and the presence of extracellular  $\text{Cl}^-$  as shown in Figure 1 (see also [49]).
2. Intracellular  $\text{Cl}^-$  plays no role in TMEM16A activation. This observation is based on experiments where the  $V_m$ -dependence of TMEM16A was nearly identical in the presence of 40 and 88 mM  $[\text{Cl}^-]_i$  (data not shown).
3. TMEM16A can be activated in a cooperative way by  $V_m$ , intracellular  $\text{Ca}^{2+}$ , and  $\text{Cl}^-$  (Figures 2 and 3).
4. The interaction between intracellular  $\text{Ca}^{2+}$  and TMEM16A is a  $V_m$ -dependent process [49].
5. Binding of at least 2  $\text{Ca}^{2+}$  ions activates TMEM16A as suggested by dose-response curves and structural data [5, 17, 35, 49, 52].
6. Binding of the two  $\text{Ca}^{2+}$  ions occurs in a sequential manner with the same single site-affinity.

Activation of TMEM16A by  $V_m$  in cells dialyzed with 0  $\mu\text{M}$   $[\text{Ca}^{2+}]_i$  (Figure 1) was described as a simple closed-open ( $C \rightleftharpoons O$ ) transition. This condition is represented by Scheme I in Figure 4 where  $\alpha_1$  and  $\beta_1$  are forward and backward rate constants (Equation 4) that change exponentially with  $V_m$  [15, 16].

In the presence of  $\text{Cl}^-$ , a channel dwelling in C or O states can bind  $\text{Cl}^-$  and move into  $C_{\text{Cl}}$  and  $C_{\text{Cl}}O$  states (see Scheme II(A) in Figure 4). The rate constants  $[\text{Cl}^-]_o k_{\text{CCl1}}$ ,  $k_{\text{CCl2}}$ ,  $[\text{Cl}^-]_o k_{\text{OCl1}}$ , and  $k_{\text{OCl2}}$  control the  $C \rightleftharpoons C_{\text{Cl}}$  and  $O \rightleftharpoons C_{\text{Cl}}O$  transitions in the presence of external  $\text{Cl}^-$ , while  $\alpha_{\text{Cl1}}$  and  $\beta_{\text{Cl1}}$  control the  $C_{\text{Cl}} \rightleftharpoons C_{\text{Cl}}O$  transitions. A subsequent increase in intracellular  $\text{Ca}^{2+}$  will drive the channel into one of the following states:  $C \rightleftharpoons C_{\text{Ca}}$ ,  $O \rightleftharpoons C_{\text{Ca}}O$ ,  $C_{\text{Cl}} \rightleftharpoons C_{\text{Cl}}C_{\text{Ca}}$  and  $C_{\text{Cl}}O \rightleftharpoons C_{\text{Cl}}OC_{\text{Ca}}$  (see Scheme III(A), Figure 4). These transitions are controlled by forward rate constants  $[\text{Ca}^{2+}]_i k_{\text{C1}}$ ,  $[\text{Ca}^{2+}]_i k_{\text{C1Cl}}$ ,  $[\text{Ca}^{2+}]_i k_{\text{O1Cl}}$  and  $[\text{Ca}^{2+}]_i k_{\text{O1}}$  and backward rate constants  $k_{\text{C2}}$ ,  $k_{\text{C2Cl}}$ ,  $k_{\text{O2Cl}}$  and  $k_{\text{O2}}$  (described by Equation 4). Previous fast perfusion experiments show that upon  $\text{Ca}^{2+}$  removal the current deactivates in a  $V_m$ -dependent manner [49]. Therefore, only the rate constants controlling unbinding of  $\text{Ca}^{2+}$ ,  $k_{\text{O2}}$ ,  $k_{\text{C2}}$ ,  $k_{\text{C2Cl}}$  and  $k_{\text{O2Cl}}$  are  $V_m$ -dependent. The rate constants controlling  $\text{Ca}^{2+}$ -binding are  $V_m$ -independent. Depending on their permeability anions can facilitate channel activation [36] and decrease the amount of  $\text{Ca}^{2+}$  needed to produce half-maximum activation [4, 39]. Based on this we introduced an effect of  $\text{Ca}^{2+}$  on the rate constants ( $k_{\text{CCl}}$  and  $k_{\text{OCl}}$ )

controlling the  $C \rightleftharpoons C_{Cl}$  and  $O \rightleftharpoons C_{Cl}O$  transitions. This effect of  $Ca^{2+}$  is represented in the model by weight parameters  $I, L, h, H, m$  and  $M$ . Table 2B lists the relationship between rate constants and weight factors. Finally, the  $Ca^{2+}$  dose-response curves suggest that at least two  $Ca^{2+}$  are needed to activate TMEM16A [2, 27, 35, 47, 49, 52]. The binding of an additional  $Ca^{2+}$  to the channels leads to Scheme IV. In this new scheme we presuppose that: 1) the open and closed state can bind  $Ca^{2+}$  with different affinity, and 2) within each state both  $Ca^{2+}$  ions bind with the same single site affinity.

Alternatively, when both intracellular  $Ca^{2+}$  and  $Cl^-$  are present, a channel dwelling between C and O states (Scheme I) can bind two  $Ca^{2+}$  ions to move into Schemes II(B) and III(B), respectively. The transitions between C and O states are controlled by rate constants  $[Ca^{2+}]_i k_{C1}, k_{C2}, [Ca^{2+}]_i k_{O1}$  and  $k_{O2}$ . Next binding of one external  $Cl^-$  to channels in Scheme III(B) leads to Scheme IV. Note that binding of just one  $Cl^-$  by channels represented in Scheme II(B) leads to Scheme III(A). Since  $Cl^-$  permeates through the channel, then we do not expect that all cycles of Scheme IV will satisfy microscopic reversibility. Cycles represented with states connected by wider arrows did not satisfy the reversibility principle.

The models depicted by Schemes III(A) and IV take into account the contribution of  $V_m$ ,  $Ca^{2+}$ , and  $Cl^-$  to gating and hence can be used to describe the properties of TMEM16A. To test them we performed a global fit of data describing the  $V_m$ ,  $Ca^{2+}$ , and  $Cl^-$  dependence of gating. The experimental data used in the global fits included:

1.  $I_{Cl}$  vs  $V_m$  curves obtained from cells dialyzed with 0  $Ca^{2+}$  and 40 mM  $Cl^-$  and bathed in 140 mM or 30 mM  $Cl^-$ .
2. Mean  $I_{Cl}$  traces obtained from cell dialyzed with  $[Ca^{2+}]_i = 0, 0.2$  and 1  $\mu M$  and stepped to  $V_m$  ranging from  $-100$  mV to 160 mV.
3. Representative  $I_{Cl}$  traces obtained by fast perfusion of 20  $\mu M$   $[Ca^{2+}]_i$  to excised patches held at  $V_m$  from  $-100$  mV to 100 mV in 20 mV increments.
4. Mean  $I_{Cl}$  recordings obtained from cells sequentially exposed to 1 mM, 10 mM and 140mM  $[Cl^-]_o$ .
5. Mean  $I_{Cl}$  recordings obtained from cells dialyzed with 0.2  $\mu M$   $[Ca^{2+}]_i$  and 40 mM  $[Cl^-]_i$  while bathed in 140 mM or 30 mM  $[Cl^-]_o$  and depolarized to  $-20$  mV to  $+120$  mV for 20 s.

The inclusion of such a wide range of data in the global fit constrained the value for the rate constants and ensured the robustness of our model. The model depicted in Scheme III(A), which included only one  $Ca^{2+}$  bound, partially reproduced TMEM16A activation. It was not able to describe activation at very high  $[Ca^{2+}]_i$ , the kinetics of tail currents in cells dialyzed with 1  $\mu M$   $Ca^{2+}$ , or  $I_{Cl}$  generated with 20 s pulses from cells exposed to 30 mM  $Cl^-$  (Supplemental Figures 1 and 2). In contrast, Scheme IV, which included two  $Ca^{2+}$  ions bound, described the data reasonably well. The results are shown in Figures 5 and 6 as solid black traces (fits) superimposed on the experimental data (grey lines). Figures 5 A, B and C show fits of Scheme IV to  $I_{Cl}$  recorded from different cells dialyzed with 0, 0.2 and 1  $\mu M$   $[Ca^{2+}]_i$ . Figure 5D displays the fits of  $I_{Cl}$  generated by rapid perfusion with 20  $\mu M$   $[Ca^{2+}]_i$  to inside-out patches held from  $-100$  mV to  $+100$  mV. The model fit the entire traces nicely.

The model was able to fit the fast onset of the currents recorded at 0  $[Ca^{2+}]_i$  (inset in A), the fast tail currents recorded with 0.2  $\mu M$   $Ca^{2+}$  (inset in B) and the fast on and off time courses of the current activated with 20  $\mu M$   $Ca^{2+}$ . However, the model did not describe well the tail current recorded with 1  $\mu M$   $Ca^{2+}$  (inset in C). Similarly, Scheme IV was able to fit the  $I_{Cl}-V_m$  relationships obtained from cells exposed to 30 and then 140 mM  $[Cl^-]_o$  in the absence of intracellular  $Ca^{2+}$  (Figure 6A, grey and black circles) and the  $I_{tail}$  recorded from different cells exposed to 10 and 1 mM  $[Cl^-]_o$ , dialyzed with 0.2  $\mu M$   $[Ca^{2+}]_i$  and 40 mM  $[Cl^-]_i$  (Figure 6B). Scheme IV also fitted the mean  $I_{Cl}$  recorded with 20 s depolarizations from cells exposed to 30 mM and 140 mM  $[Cl^-]_o$  and dialyzed with 0.2  $\mu M$   $[Ca^{2+}]_i$  and 40 mM  $[Cl^-]_i$  (Figure 6C). Here we can see that the model described quite well  $I_{Cl}$  recorded in the presence of 140 mM  $Cl^-$  but not 30 mM  $Cl^-$ . Fast components, such as the tail currents (right insets in B and C) at both  $[Cl^-]$  were well described. The overall global fit goodness of the model with the binding of  $Ca^{2+}$  to two sites with the same affinity ( $k_{O2}/k_{O1}$ ), given by the regression coefficient ( $R^2$ ) associated with the minimization process had a value of 0.98 (Equation 5). We also tested the alternative model that considers different  $Ca^{2+}$  affinities for the two  $Ca^{2+}$  binding sites:  $k_{O2}/k_{O1}$  for the first site and  $c^* k_{O2}/k_{O1}$ , for the second site, where  $c$  is a constant parameter. This model fits the data with the same  $R^2=0.98$  as that obtained with Scheme IV with two sites with the same affinity. However, the binding affinities only varied by a factor of 0.61 and the  $V_m$ -dependence of  $EC_{50}$  was indistinguishable from that obtained assuming the same affinity. Therefore, we consider that Scheme IV with two  $Ca^{2+}$  binding sites with the same affinity was a reasonable model of TMEM16A and can be used to obtain the rate constant parameters and the apparent charge ( $z$ ) values for Scheme IV. Table 2 lists these values. The  $z$  values indicate that most of the  $V_m$ -dependence is conferred by: a) the charge transferred during the  $Ca^{2+}$  unbinding steps controlled by  $k_{O2}$  ( $z=0.168$ ), b) the transition  $C_{Cl} \rightleftharpoons O_{Cl}$  controlled by  $\alpha_{C11}$  ( $z=0.11$ ) and  $\beta_{C11}$  ( $z=0.32$ ), and c) the  $Cl^-$  binding steps to C or O conformations controlled by  $k_{CC11}$  ( $z=0.2$ ) and  $k_{OC1}$  ( $z=0.65$ ), respectively.

If these global fits are a realistic representation of TMEM16A gating, then Scheme IV plus the set of parameter values listed in Table 2 should be able to predict the quasi-steady-state properties of TMEM16A. These properties include  $I_{Cl}-V_m$  curves,  $Ca^{2+}$  dose-response curves, and the  $V_m$ -dependence of  $EC_{50}$  and the Hill coefficient. We chose these fingerprint properties because they have been well characterized by different laboratories [2, 19, 27, 31, 32, 35]. Our approach consisted of simulating TMEM16A currents under different  $[Ca^{2+}]_i$  and  $V_m$  using IonChannelLab software [44] as described in Methods. Then we used the simulated  $I_{Cl}$  to construct  $I_{Cl}-V_m$  curves and  $Ca^{2+}$  dose-response curves. To make a stringent comparison, we compared the simulated properties to previously published data [49]. Data was from cells dialyzed with  $[Ca^{2+}]_i$  ranging from 0 to 6.5  $\mu M$ , and stimulated with 0.7 s pulses from  $-100$  mV to  $+100$  mV. Figure 7 shows superimposed experimental data (black symbols) and model predictions (solid lines) for  $I_{Cl}$  vs  $V_m$  relationships at the indicated  $[Ca^{2+}]_i$  (Figure 7A), dose-response curves to  $[Ca^{2+}]_i$  at different  $V_m$  (Figure 7B), and  $V_m$ -dependence of  $EC_{50}$  and the Hill coefficient  $n_H$  (Figure 7C). These properties of TMEM16A, except the  $EC_{50}$ , were adequately predicted by Scheme IV and its associated rate constants. Nevertheless, the  $EC_{50}$  value predicted by the model at  $+60$  mV/140 mM

$[Cl^-]_o$  was 0.85  $\mu M$ , which is within the range of values determined experimentally [2, 17, 22, 35, 49].

Finally, it has been shown that anions more permeable than  $Cl^-$  modify CaCC and TMEM16A gating [36, 49]. Importantly, anions more permeable than  $Cl^-$  increase the apparent  $Ca^{2+}$  sensitivity of TMEM16A and TMEM16B [4, 39]. In this work, we show that increasing  $[Cl^-]_o$  facilitates gating, but whether or not this effect is due to an increased  $Ca^{2+}$  sensitivity is unknown. Therefore, we used the model to predict whether extracellular  $Cl^-$  regulates TMEM16A gating by altering its  $Ca^{2+}$  or voltage sensitivity. Dose-response curves to  $Ca^{2+}$  were calculated using Scheme IV with 140 mM or 30 mM  $[Cl^-]_o$  and  $V_m = +60/-60$  mV. The model predicts that neither the apparent  $Ca^{2+}$  sensitivity nor the  $V_m$ -dependence of  $EC_{50}$  are altered by decreasing  $[Cl^-]_o$ . To determine whether this prediction is true, we determined the dose-response curves to  $Ca^{2+}$  for TMEM16A using inside-out patches held at  $\pm 60$  and  $\pm 80$  mV in 140 mM or 30 mM  $[Cl^-]_o$ . Figures 8A and 8B show typical raw  $I_{Cl}$  traces obtained from two different patches bathed in 140 mM (A) and 30 mM (B)  $Cl^-$  while the  $[Ca^{2+}]_i$  was changed between zero and the concentrations indicated by the small letters. Upward deflections are records obtained at +60 mV while downward deflections are records obtained at -60 mV. Clearly  $I_{Cl}$  at +60 mV saturated when  $[Ca^{2+}]_i$  was around 5–12  $\mu M$  regardless of the  $[Cl^-]_o$  present. At -60 mV,  $I_{Cl}$  nearly saturated with 12  $\mu M$   $[Ca^{2+}]_i$ . Figure 8C shows the resulting dose-response curves at +60 mV (left) and at -60 mV (right). The data (black and grey circles) nicely matched the values predicted by Scheme IV (solid lines). Furthermore, the predicted  $V_m$ -dependence of  $EC_{50}$  was also matched by the experimental data (continuous lines and symbols in Figure 8D). The  $EC_{50}$  value of 0.85  $\mu M$  predicted by the model at +60 mV and 140 mM  $[Cl^-]_o$  was similar to those experimentally reported: 1.5, 1.3, 0.4, 1.5, and  $0.79 \pm 0.05$   $\mu M$  [27, 46, 48, 49, this work]. Taken together these results demonstrate that external  $Cl^-$  does not alter  $Ca^{2+}$ -sensitivity in TMEM16A. The fact that our kinetic model predicted this result is a good indication of the model robustness and that the model includes critical information about the mechanism of TMEM16A gating.

### Activation pathways

Since Scheme IV was able to reproduce the activation properties of TMEM16A, we decided to apply the model to determine what would be the most likely pathway(s) followed by TMEM16A during the activation process. For this purpose, we calculated the probability (P) that TMEM16A visited each of the 12 states when intracellular  $Ca^{2+}$ , external  $Cl^-$ , and  $V_m$  were varied (Supplemental material). To obtain a gating pathway we determined the most likely state to be occupied once the channel visited a given state. For example, when the channel visits state C, it can go to O,  $C_{Cl}$  or  $C_{Ca}$  states. Our P value calculations indicated that state  $C_{Ca}$  was the most likely state to be occupied. We repeated this strategy to find the next most probable state to be visited until the channel reached  $ClO_2Ca$ . First, we consider activation of TMEM16A by a 0.5 s depolarization to +120 mV followed by repolarization to -60 mV when  $[Ca^{2+}]_i = 0$ ,  $[Cl^-]_i = 40$  mM and  $[Cl^-]_o$  changed between 140 mM and 30 mM. This condition is represented by the pink kinetic scheme box in Figure 9C. The time-dependent P values for states C, O,  $C_{Cl}$ , and  $ClO$  are shown in Figure 9A.  $P_C$ ,  $P_O$ ,  $P_{C_{Cl}}$  and  $P_{ClO}$  values were 0.782, 0, 0.217 and 0.0008, when  $[Cl^-]_o$  was 140 mM. After external  $Cl^-$  was decreased to 30 mM  $P_C$  increased to 0.941, while  $P_{C_{Cl}}$  and  $P_{ClO}$  fell to 0.057 and

0.0002, respectively. Thus, in the absence of intracellular  $\text{Ca}^{2+}$  the most likely gating route is  $\text{C} \rightarrow \text{C}_{\text{Cl}} \rightarrow \text{C}_{\text{ClO}}$  (Figure 9C, blue and pink arrows).

Subsequently, P values were calculated when  $[\text{Ca}^{2+}]_i$  was 0.2  $\mu\text{M}$ ,  $[\text{Cl}^-]_o$  was either 140 or 30 mM,  $[\text{Cl}^-]_i = 40$  mM, and  $V_m$  was +120 mV during 20 s followed by repolarization to -60 mV. These experimental conditions are the same as the ones used for collecting data shown in Figure 3C (right) and data collected using short depolarizations. Figure 9B shows P values for states in the inner circle (pink), middle circle (white), and outer circle (grey), respectively. When  $[\text{Cl}^-]_o$  was 140 mM (left column), the depolarization induced an abrupt decrease of  $P_{\text{C}}$ , followed by a further exponential decrease. Such decrease was mirrored by an abrupt increase and then exponential decrease in  $P_{\text{CCa}}$ . At the same time,  $P_{\text{C}_{\text{ClO}}\text{Ca}}$  and  $P_{\text{C}_{2\text{Ca}}}$  increased little, and  $P_{\text{O}_{2\text{Ca}}}$  increased transiently. Notably,  $P_{\text{C}_{\text{ClO}}\text{O}_{2\text{Ca}}}$  increased steadily reaching 0.4 by the end of the 20 s depolarization. The same trend was observed when  $[\text{Cl}^-]_o$  was 30 mM, albeit the magnitude of P for each state declined. Interestingly, during the first 2 s into the depolarization  $P_{\text{C}_{\text{Cl}}\text{C}}$  decreased but then increased in a time-dependent manner. In summary, in the presence of 0.2  $\mu\text{M}$   $[\text{Ca}^{2+}]_i$  and 140 mM or 30 mM  $[\text{Cl}^-]_o$ , TMEM16A activation proceeded following two pathways. At early times (<2 s), the route  $\text{C} \rightarrow \text{C}_{\text{Ca}} \rightarrow \text{C}_{2\text{Ca}} \rightarrow \text{O}_{2\text{Ca}} \rightarrow \text{C}_{\text{ClO}}\text{O}_{2\text{Ca}}$  (black arrow) was preferred. However, as depolarization continued, the route  $\text{C} \rightarrow \text{C}_{\text{Cl}}\text{C} \rightarrow \text{C}_{\text{Cl}}\text{C}_{\text{Ca}} \rightarrow \text{C}_{\text{Cl}}\text{O}_{\text{Ca}} \rightarrow \text{C}_{\text{Cl}}\text{O}_{2\text{Ca}}$  (green arrow) also contributed to the total current. The effect of lowering  $[\text{Cl}^-]_o$  to 30 mM was to decrease the contribution of both routes to the total current (grey and light green arrows). From these calculations, we observed that the greatest contribution to the total current is given by the active states  $_{\text{Ca}}\text{O}_{\text{Cl}}$ ,  $_{2\text{Ca}}\text{O}$  and  $_{2\text{Ca}}\text{O}_{\text{Cl}}$ . Therefore the net effect of increasing chloride from 30 to 140 mM was to increase  $P_{_{\text{Ca}}\text{O}_{\text{Cl}}}$  and  $P_{_{2\text{Ca}}\text{O}_{\text{Cl}}}$ .

## DISCUSSION

CaCC gating is a complex process; it involves the combined action of  $V_m$ ,  $\text{Ca}^{2+}$  and  $\text{Cl}^-$ . Several kinetic models have been previously proposed to explain the  $V_m$  and  $\text{Ca}^{2+}$ -dependence of CaCC gating [2, 20, 27]. However, these early models assumed an initial  $\text{Ca}^{2+}$ -dependent  $\text{C} \rightleftharpoons \text{C}_{\text{Ca}}$  transition and did not consider a  $\text{C} \rightleftharpoons \text{O}$  transition in the absence of  $\text{Ca}^{2+}$  or the role of external  $\text{Cl}^-$  in gating. These models predict an open probability of zero at any  $V_m$  if  $[\text{Ca}^{2+}]_i = 0$ , which is not the case for TMEM16A [49]. In this work, we present an alternative kinetic model that satisfactorily accounts for the  $V_m$ ,  $\text{Ca}^{2+}$ , and  $\text{Cl}^-$ -dependent gating of TMEM16A channel. We propose that the gating of the TMEM16A  $\text{Cl}^-$  channel is caused by consecutive direct  $V_m$ -dependent binding of two intracellular  $\text{Ca}^{2+}$  ions, coupled to a  $V_m$ -dependent binding of external  $\text{Cl}^-$ . External  $\text{Cl}^-$  facilitates gating by binding to a  $\text{Ca}^{2+}$ -free closed state and favouring the transition to  $\text{Ca}^{2+}$ -bound open states. By means of facilitating the  $_{2\text{Ca}}\text{O} \rightleftharpoons _{2\text{Ca}}\text{O}_{\text{Cl}}$  transition, external  $\text{Cl}^-$  induces the slow gating [11]. In our model (Scheme IV) the direct  $\text{Ca}^{2+}$ -binding is controlled by forward rate constants that are independent of voltage and  $V_m$ -dependent backward rate constants. The off-rate constant measured from simulations with the model predicted that  $\text{Ca}^{2+}$  remains attached to the channel at depolarized voltages. This coincides with experimental data showing that at depolarized  $V_m$  the rate of current decay—due to  $\text{Ca}^{2+}$  washout—is very slow compared to that observed at negative  $V_m$ . Also, increasing the  $[\text{Ca}^{2+}]_i$  decreases the off rate of whole cell currents at negative potentials [2, 27, 52]. Such data show that  $\text{Ca}^{2+}$

unbinding is a  $V_m$ -dependent phenomenon [19, 27, 35, 49, 52]. Thus, the open state is stabilized when  $Ca^{2+}$  is high, and/or  $V_m$  is depolarized.

The model is not perfect. It cannot describe well  $I_{tail}$  recorded with  $1 \mu M Ca^{2+}$  and  $I_{Cl}$  recorded in the presence of  $30 mM Cl^-$  using  $20 s$  depolarizations. Also, the  $EC_{50}$  is not adequately predicted by Scheme IV. There are different possibilities to explain these discrepancies. The rate constants are relatively simple; they are exponential functions of  $V_m$  and depended linearly on  $[Cl^-]_o$ . However, such dependence could be state dependent and/or be more complicated. The weight factors ( $l$ ,  $L$ ,  $h$ ,  $H$ ,  $m$ , and  $M$ ) are assumed to be constant and we considered that only one  $Cl^-$  ion is needed affect channel gating without affecting the single channel conductance. These assumptions may not hold under all experimental conditions. Finally, for simplicity, we assumed that  $Ca^{2+}$  binds to two sites with a single binding affinity which we call single-site affinity. This may not be the case as suggested by mutagenesis experiments which show that mutations located in different parts of the protein alter  $Ca^{2+}$  sensitivity [17, 47, 49, 52]. Inadequacies of one or all these variables would hinder the ability of the model to reproduce the data. Refining the model to include the exact number of  $Ca^{2+}$  binding sites, their binding affinity and allosteric interactions with  $Cl^-$  would be more realistic as more structural data becomes available. In addition, our model ignores the permeation process. Including this property would be necessary to understand the effects of pore occupancy by permeant anions on channel gating [4, 36, 39]. Despite these limitations, Scheme IV predicted no change in the apparent  $Ca^{2+}$  affinity of TMEM16A when  $[Cl^-]_o$  was lowered from  $140 mM$  to  $30 mM$ , and this prediction was successfully corroborated experimentally. The model also predicts that a small fraction of the charge ( $z_2 = 0.17$ ) is transferred during the  $Ca^{2+}$  unbinding steps. This number agrees with the small  $V_m$ -dependence of the dose-response curves to  $[Ca^{2+}]_i$  [2, 22, 35, 49]. We consider that Scheme IV was effective because a large data set was used to extract the rate constant parameters. This tactic largely constrained the possible values of the rate constant parameters and contributed to enhance the robustness of the model.

The effect of external  $Cl^-$  on CaCCs is maybe more complex than previously anticipated since our data show that varying external  $Cl^-$  alters both the fast and slow gating modes of TMEM16A and TMEM16B [11]. In addition, our model-dependent calculations using the rate constants listed in Table 2 revealed that external  $Cl^-$  ion plays a significant role on  $V_m$ -dependent activation in the absence of  $Ca^{2+}$ . Under this condition, there is a substantial amount of charge transferred during the  $Cl^-$  binding steps to either C or O conformations as indicated by  $z_{+Cl} = 0.2$  and  $z_{+O} = 0.65$  (Table 2A). The binding of one  $Cl^-$  to the C conformation of the channel prompts its conversion into  $C_1C$  and subsequently the  $C_1O$  state. The later transition is also accompanied by charge transferred as indicated by  $z_{11} = 0.11$  and  $z_{12} = 0.33$  (Table 2). The  $C_1O$  state would enable  $Cl^-$  conductance in the absence of intracellular  $Ca^{2+}$ . Furthermore, when  $Ca^{2+}$  is bound to the channel the external  $Cl^-$  favours the  ${}_{2Ca}O \rightleftharpoons {}_{2Ca}OCl$  transition and so the slow component of channel gating arises. In fact, by increasing  $[Cl^-]_o$  from  $30 mM$  to  $140 mM$  in the presence of  $0.2 \mu M [Ca^{2+}]_i$  we observed an increase in  $P_{{}_{2Ca}OCl} + P_{{}_{Ca}OCl}$  from  $0.08$  to  $0.22$ , suggesting that  $Ca^{2+}$  remains bound to the channel for a longer time. Also, an increased occupation of the  ${}_{2Ca}OCl$  state implies a longer dwell time of the channel in this state. High  $[Cl^-]_o$  shifted to negative values the  $V_m$ -dependence of occupation for the  ${}_{2Ca}OCl$  state such that at a given  $V_m$  the probability of

occupation is increased with high  $[Cl^-]_o$ . Despite these changes, the overall apparent affinity of TMEM16A for  $Ca^{2+}$  was not altered. However, previous experimental observations suggest a coupling of the permeation and gating mechanisms. For example, highly permeant anions alter the kinetics and  $EC_{50}$  as described for CaCC from mouse parotid acinar cells, *Xenopus* oocytes and TMEM16B [4, 36, 38, 39]. These data can be reconciled considering that TMEM16A may have two anion binding sites as previously suggested [38] and the external anions might alter TMEM16A gating by at least two mechanisms. One mechanism may involve permeation and gating, while another mechanism may affect only gating, similar to what we describe here. Our idea describes the effect of external  $Cl^-$  on TMEM16A based on what has been proposed for other  $Cl^-$  channels. For example, in CLC-0 and CLC-1 external anions have a profound facilitating effect on gating [7, 14, 37] and in CLC-2  $V_m$ -dependence is conferred by permeant anions that occupy and then exit the pore [25, 41]. Thus, the role of permeant anions in gating the  $Cl^-$  channels may be more important than thought in the past. More research is needed to establish the connection between permeation and gating.

TMEM16A gating shares some similarities with BK channel gating. For example, both channels display coupling between  $V_m$  and  $Ca^{2+}$  binding, both channels are activated by  $V_m$  alone, and increments in  $[Ca^{2+}]_i$  lead to a leftward shift of the  $G_{Norm}(V_m)$  curve. However, there are also differences: BK has an intrinsic  $V_m$  sensor and TMEM16A does not,  $Ba^{2+}$  activates BK channels by interacting with the  $Ca^{2+}$  binding site but  $Ba^{2+}$  also binds and blocks the conduction pathway of BK channels while  $Ba^{2+}$  only activates TMEM16A [24, 33, 34, 49, 52, 53]. Allosteric models have been successful in explaining the interaction between  $V_m$  and  $Ca^{2+}$  in the gating of BK channels [24]. Although TMEM16A gating is not exactly like the gating of BK channels, an allosteric model should be considered for TMEM16A channel.

Our findings could be relevant to TMEM16A function under physiological conditions. For example, the model could be helpful to understand the behaviour of TMEM16A during agonist-stimulated  $Ca^{2+}$ -dependent fluid secretion. Secretory epithelial cells response to agonist include an oscillatory membrane potential accompanied by oscillations in the intracellular  $[Ca^{2+}]_i$  [30]. Furthermore, during fluid and electrolyte secretion by acinar cells,  $[Cl^-]_i$  decreases from about 61 to 29 mM [18] due to  $Cl^-$  exit through TMEM16A channels [40]. Under these conditions,  $Cl^-$  would transiently increase on the extracellular side which would favour activation of TMEM16A to sustain secretion. Although the TMEM16A activation pattern may very complex under physiological conditions, it can be understood using Scheme IV.

In summary, we propose a TMEM16A gating mechanism caused by consecutive direct  $V_m$ -dependent binding of two intracellular  $Ca^{2+}$  ions, coupled to a  $V_m$ -dependent binding of one external  $Cl^-$ .

## Supplementary Material

Refer to Web version on PubMed Central for supplementary material.

## Acknowledgments

The authors thank C.Y. Hernandez-Carballo and Yuan Yuan Cui for excellent technical assistance and Kuai Yu for providing ANO1 patch clamp records for analysis. This work was supported by grants 219949 (CONACyT, Mexico) to JA. HCH is supported by grants from the National Institutes of Health GM60448, AR067786, and EY11482. JAC-V and JJ De J-P are recipients of a Graduate Student Fellowship from CONACyT, Mexico (229968 and 234820). SCR is a recipient of a Postdoctoral Fellowship from CONACyT, Mexico (256034-290807).

## References

1. Arreola J, Melvin JE, Begenisich T. Inhibition of Ca<sup>2+</sup>-dependent Cl<sup>-</sup> Channels from Secretory Epithelial Cells by Low Internal pH. *J Membr Biol.* 1995; 147:95–104. DOI: 10.1007/BF00235400 [PubMed: 8531203]
2. Arreola J, Melvin JE, Begenisich T. Activation of calcium-dependent chloride channels in rat parotid acinar cells. *J Gen Physiol.* 1996; 108:35–47. DOI: 10.1085/jgp.108.1.35 [PubMed: 8817383]
3. Arreola, J., Reyes, JP., Rosales Saavedra, T., Pérez Cornejo, P. Chloride channels activated by intracellular ligands. In: James, K., Ceri, D., editors. *Ion Channels: From Structure to Function.* Oxford University Press; 2010. p. 506-511.
4. Betto G, Cherian OL, Pifferi S, Cenedese V, Boccaccio A, Menini A. Interactions between permeation and gating in the TMEM16B/anoctamin2 calcium-activated chloride channel. *J Gen Physiol.* 2014; 143:703–18. DOI: 10.1085/jgp.201411182 [PubMed: 24863931]
5. Brunner JD, Lim NK, Schenck S, Duerst A, Dutzler R. X-ray structure of a calcium-activated TMEM16 lipid scramblase. *Nature.* 2014; 516:207–212. DOI: 10.1038/nature13984 [PubMed: 25383531]
6. Caputo A, Caci E, Ferrera L, Pedemonte N, Barsanti C, Sondo E, Pfeiffer U, Ravazzolo R, Zegarar-Moran O, Galiotta LJV. TMEM16A, a membrane protein associated with calcium-dependent chloride channel activity. *Science (80-).* 2008; 322:590–4. DOI: 10.1126/science.1163518
7. Chen TY, Miller C. Nonequilibrium gating and voltage dependence of the ClC-0 Cl<sup>-</sup> channel. *J Gen Physiol.* 1996; 108:237–250. DOI: 10.1085/jgp.108.4.237 [PubMed: 8894974]
8. Chun H, Cho H, Choi J, Lee J, Kim S, Kim H, Oh U. Protons inhibit anoctamin 1 by competing with calcium. *Cell Calcium.* 2015; 5:431–41. DOI: 10.1016/j.ceca.2015.06.011
9. Colquhoun D, Hawkes AG. Relaxation and Fluctuations of Membrane Currents that Flow through Drug-Perated Channels. *Proc R Soc Lond B Biol Sci.* 1977; 199:231–262. DOI: 10.1098/rspb.1977.0137 [PubMed: 22856]
10. Covarrubias M, Bhattacharji A, De Santiago-Castillo JA, Dougherty K, Kaulin YA, Na-Phuket TR, Wang G. The Neuronal Kv4 Channel Complex. *Neurochem Res.* 2008; 33:1558–1567. DOI: 10.1007/s11064-008-9650-8 [PubMed: 18357523]
11. Cruz Rangel S, De Jesús Pérez JJ, Contreras Vite JA, Pérez Cornejo P, Hartzell H, Arreola J. Gating modes of calcium-activated chloride channels TMEM16A and TMEM16B. *J Physiol.* 2015; 24:5283–98. DOI: 10.1113/JP271256
12. Dougherty K, De Santiago-Castillo J a, Covarrubias M. Gating Charge immobilization in Kv4.2 Channels: The Basis of Closed-State Inactivation. *J Gen Physiol.* 2008; 131:257–73. DOI: 10.1085/jgp.200709938 [PubMed: 18299396]
13. Duvvuri U, Shiwerski DJ, Xiao D, Bertrand C, Huang X, Edinger RS, Rock JR, Harfe BD, Henson BJ, Kunzelmann K, Schreiber R, Seethala RS, Egloff AM, Chen X, Lui VW, Grandis JR, Gollin SM. TMEM16A Induces MAPK and Contributes Directly to Tumorigenesis and Cancer Progression. *Cancer Res.* 2012; 72:3270–3281. DOI: 10.1158/0008-5472.CAN-12-0475-T [PubMed: 22564524]
14. Engh AM, Faraldo-Gomez JD, Maduke M. The Mechanism of Fast-Gate Opening in ClC-0. *J Gen Physiol.* 2007; 130:335–349. DOI: 10.1085/jgp.200709759 [PubMed: 17846164]
15. Eyring H. The Activated Complex in Chemical Reactions. *J Chem Phys.* 1935; 445:107–115. DOI: 10.1063/1.1749604
16. Eyring H. The Activated Complex and the Absolute Rate of Chemical Reactions. *Chem Rev.* 1935; 17:65–77. DOI: 10.1021/cr60056a006



17. Ferrera L, Caputo A, Ubbi I, Bussani E, Zegarra-Moran O, Ravazzolo R, Pagani F, Galletta LJV. Regulation of TMEM16A Chloride Channel Properties by Alternative Splicing. *J Biol Chem*. 2009; 284:33360–8. DOI: 10.1074/jbc.M109.046607 [PubMed: 19819874]
18. Foskett JK.  $[Ca^{2+}]_i$  modulation of  $Cl^-$  content controls cell volume in single salivary acinar cells during fluid secretion. *Am J Physiol*. 1990; 259:C998–C1004. [PubMed: 2260645]
19. Gomez-Hernandez JM, Stühmer W, Parekh AB. Calcium dependence and distribution of calcium-activated chloride channels in *Xenopus* oocytes. *J Physiol*. 1997; 502(Pt 3):569–74. DOI: 10.1111/j.1469-7793.1997.569bj.x [PubMed: 9279809]
20. Haase A, Hartung K. Activation and inactivation kinetics of a  $Ca^{2+}$ -activated  $Cl^-$  current: photolytic  $Ca^{2+}$  concentration and voltage jump experiments. *Pflugers Arch*. 2006; 452:81–90. DOI: 10.1007/s00424-005-0004-y [PubMed: 16283204]
21. Hartzell C, Putzier I, Arreola J. Calcium-activated chloride channels. *Annu Rev Physiol*. 2005; 67:719–758. DOI: 10.1146/annurev.physiol.67.032003.154341 [PubMed: 15709976]
22. Hartzell HC, Qu Z. Chloride Currents in Acutely Isolated *Xenopus* Retinal Pigment Epithelial Cells. *J Physiol*. 2003; 549:453–69. DOI: 10.1113/jphysiol.2003.040428 [PubMed: 12665603]
23. Hernández-Carballo CY, De Santiago-Castillo JA, Rosales-Saavedra T, Pérez-Cornejo P, Arreola J. Control of volume-sensitive chloride channel inactivation by the coupled action of intracellular chloride and extracellular protons. *Pflugers Arch Eur J Physiol*. 2010; 460:633–644. DOI: 10.1007/s00424-010-0842-0 [PubMed: 20454973]
24. Horrigan FT, Aldrich RW. Coupling between voltage sensor activation,  $Ca^{2+}$  binding and channel opening in large conductance (BK) potassium channels. *J Gen Physiol*. 2002; 120:267–305. DOI: 10.1085/jgp.20028605 [PubMed: 12198087]
25. De Jesús Pérez JJ, Castro-Chong A, Shieh R, Hernández Carballo CY, de Santiago Castillos JA, Arreola J. Gating the glutamate gate of CLC-2 chloride channel by pore occupancy. *J Gen Physiol*. 2016; 1:25–37. DOI: 10.1085/jgp.201511424
26. Korn SJ, Horn R. Statistical discrimination of fractal and markov models of single-channel gating. *Biophys J*. 1988; 54:871–877. DOI: 10.1016/S0006-3495(88)83023-6 [PubMed: 2468367]
27. Kuruma A, Hartzell HC. Bimodal Control of a  $Ca^{2+}$ -Activated  $Cl^-$  Channel by Different  $Ca^{2+}$  Signals. *J Gen Physiol*. 2000; 115:59–80. DOI: 10.1085/jgp.115.1.59 [PubMed: 10613919]
28. Lape R, Colquhoun D, Sivilotti LG. On the nature of partial agonism in the nicotinic receptor superfamily. *Nature*. 2008; 454:722–7. DOI: 10.1038/nature07139 [PubMed: 18633353]
29. Large WA, Wang Q. Characteristics and physiological role of the  $Ca^{2+}$ -activated  $Cl^-$  conductance in smooth muscle. *Am J Physiol*. 1996; 271:C435–C454. doi: C435–C454. [PubMed: 8769982]
30. Melvin JE, Yule D, Shuttleworth T, Begenisich T. Regulation of fluid and electrolyte secretion in salivary gland acinar cells. *Annu Rev Physiol*. 2005; 67:445–469. DOI: 10.1146/annurev.physiol.67.041703.084745 [PubMed: 15709965]
31. Miledi R. A Calcium-Dependent Transient Outward Current in *Xenopus laevis* Oocytes. *Proc R Soc Lond B Biol Sci*. 1982; 215:491–497. DOI: 10.1098/rspb.1982.0056 [PubMed: 6127718]
32. Miledi R, Parker I. Chloride current induced by injection of calcium into *Xenopus* oocytes. *J Physiol*. 1984; 357:173–83. DOI: 10.1113/jphysiol.1984.sp015495 [PubMed: 6096530]
33. Neyton J, Miller C. Potassium blocks barium permeation through a calcium-activated potassium channel. *J Gen Physiol*. 1988; 92:549–67. DOI: 10.1085/jgp.92.5.549 [PubMed: 3235973]
34. Ni YL, Kuan AS, Chen TY. Activation and Inhibition of TMEM16A Calcium-Activated Chloride Channels. *PLoS One*. 2014; 9:e86734. doi: 10.1371/journal.pone.0086734 [PubMed: 24489780]
35. Nilius B, Prenen J, Voets T, Van Den Brecht K, Eggermont J, Droogmans G. Kinetic and pharmacological properties of the calcium-activated chloride-current in macrovascular endothelial cells. *Cell Calcium*. 1997; 22:53–63. DOI: 10.1016/S0143-4160(97)90089-0 [PubMed: 9232352]
36. Perez-Cornejo P, De Santiago JA, Arreola J. Permeant Anions Control Gating of Calcium-dependent Chloride Channels. *J Membr Biol*. 2004; 198:125–33. DOI: 10.1007/s00232-004-0659-x [PubMed: 15216414]
37. Pusch M, Ludewig U, Rehfeldt A, Jentsch TJ. Gating of the voltage-dependent chloride channel  $ClC-0$  by the permeant anion. *Nature*. 1995; 373:527–531. DOI: 10.1038/373527a0 [PubMed: 7845466]

38. Qu Z, Hartzell HC. Anion Permeation in  $\text{Ca}^{2+}$ -Activated  $\text{Cl}^-$  Channels. *J Gen Physiol.* 2000; 116:825–844. DOI: 10.1085/jgp.116.6.825 [PubMed: 11099350]
39. Reyes JP, López-Rodríguez A, Espino-Saldaña AE, Huanosta-Gutiérrez A, Miledi R, Martínez-Torres A. Anion permeation in calcium-activated chloride channels formed by TMEM16A from *Xenopus tropicalis*. *Pflugers Arch Eur J Physiol.* 2014; 466:1769–1777. DOI: 10.1007/s00424-013-1415-9 [PubMed: 24352628]
40. Romanenko VG, Catalán MA, Brown DA, Putzier I, Hartzell HC, Marmorstein AD, Gonzalez-Begne M, Rock JR, Harfe BD, Melvin JE. Tmem16A encodes the  $\text{Ca}^{2+}$ -activated  $\text{Cl}^-$  channel in Mouse Submandibular Salivary Gland Acinar Cells. *J Biol Chem.* 2010; 285:12990–13001. DOI: 10.1074/jbc.M109.068544 [PubMed: 20177062]
41. Sánchez-Rodríguez JE, De Santiago-Castillo JA, Arreola J. Permeant anions contribute to voltage dependence of CIC-2 chloride channel by interacting with the protopore gate. *J Physiol.* 2010; 588:2545–56. DOI: 10.1113/jphysiol.2010.189175 [PubMed: 20498235]
42. Sánchez-Rodríguez JE, De Santiago-Castillo JA, Contreras-Vite JA, Nieto-Delgado PG, Castro-Chong A, Arreola J. Sequential interaction of chloride and proton ions with the fast gate steer the voltage-dependent gating in CIC-2 chloride channels. *J Physiol.* 2012; 590:4239–53. DOI: 10.1113/jphysiol.2012.232660 [PubMed: 22753549]
43. Sansom MS, Ball FG, Kerry CJ, McGee R, Ramsey RL, Usherwood PNR. Markov, fractal, diffusion, and related models of ion channel gating: A comparison with experimental data from two ion channels. *Biophys J.* 1989; 56:1229–1243. DOI: 10.1016/S0006-3495(89)82770-5 [PubMed: 2482085]
44. Santiago-Castillo JA, Covarrubias M, Sánchez-Rodríguez JE, Perez-Cornejo P, Arreola J. Simulating complex ion channel kinetics with IonChannelLab. *Channels (Austin).* 2010; 4:422–8. DOI: 10.4161/chan.4.5.13404 [PubMed: 20935453]
45. Schroeder BC, Cheng T, Jan YN, Jan LY. Expression Cloning of TMEM16A as a Calcium-Activated Chloride Channel Subunit. *Cell.* 2008; 134:1019–1029. DOI: 10.1016/j.cell.2008.09.003 [PubMed: 18805094]
46. Terashima H, Picollo A, Accardi A. Purified TMEM16A is sufficient to form  $\text{Ca}^{2+}$ -activated  $\text{Cl}^-$  channels. *Proc Natl Acad Sci U S A.* 2013; 110:19354–9. DOI: 10.1073/pnas.1312014110 [PubMed: 24167264]
47. Tien J, Peters CJ, Wong XM, Cheng T, Jan YN, Jan LY, Yang H. A comprehensive search for calcium binding sites critical for TMEM16A calcium-activated chloride channel activity. *Elife.* 2014; 3:1–19. DOI: 10.7554/eLife.02772
48. Vandenberg CA, Bezanilla F. A sodium channel gating model based on single channel, macroscopic ionic, and gating currents in the squid giant axon. *Biophys J.* 1991; 60:1511–1533. DOI: 10.1016/S0006-3495(91)82186-5 [PubMed: 1663796]
49. Xiao Q, Yu K, Perez-Cornejo P, Cui Y, Arreola J, Hartzell HC. Voltage- and calcium-dependent gating of TMEM16A/Ano1 chloride channels are physically coupled by the first intracellular loop. *Proc Natl Acad Sci U S A.* 2011; 108:8891–8896. DOI: 10.1073/pnas.1102147108 [PubMed: 21555582]
50. Yang YD, Cho H, Koo JY, Tak MH, Cho Y, Shim W-S, Park SP, Lee J, Lee B, Kim B-M, Raouf R, Shin YK, Oh U. TMEM16A confers receptor-activated calcium-dependent chloride conductance. *Nature.* 2008; 455:1210–5. DOI: 10.1038/nature07313 [PubMed: 18724360]
51. Yeh HI, Yeh JT, Hwang TC. Modulation of CFTR gating by permeant ions. *J Gen Physiol.* 2015; 145:47–60. DOI: 10.1085/jgp.201411272 [PubMed: 25512598]
52. Yu K, Duran C, Qu Z, Cui YY, Hartzell HC. Explaining Calcium-Dependent Gating of Anoctamin-1 Chloride Channels Requires a Revised Topology. *Circ Res.* 2012; 110:990–999. DOI: 10.1161/CIRCRESAHA.112.264440 [PubMed: 22394518]
53. Zhou Y, Zeng XH, Lingle CJ. Barium ions selectively activate BK channels via the  $\text{Ca}^{2+}$ -bowl site. *Proc Natl Acad Sci.* 2012; 109:11413–11418. DOI: 10.1073/pnas.1204444109 [PubMed: 22733762]

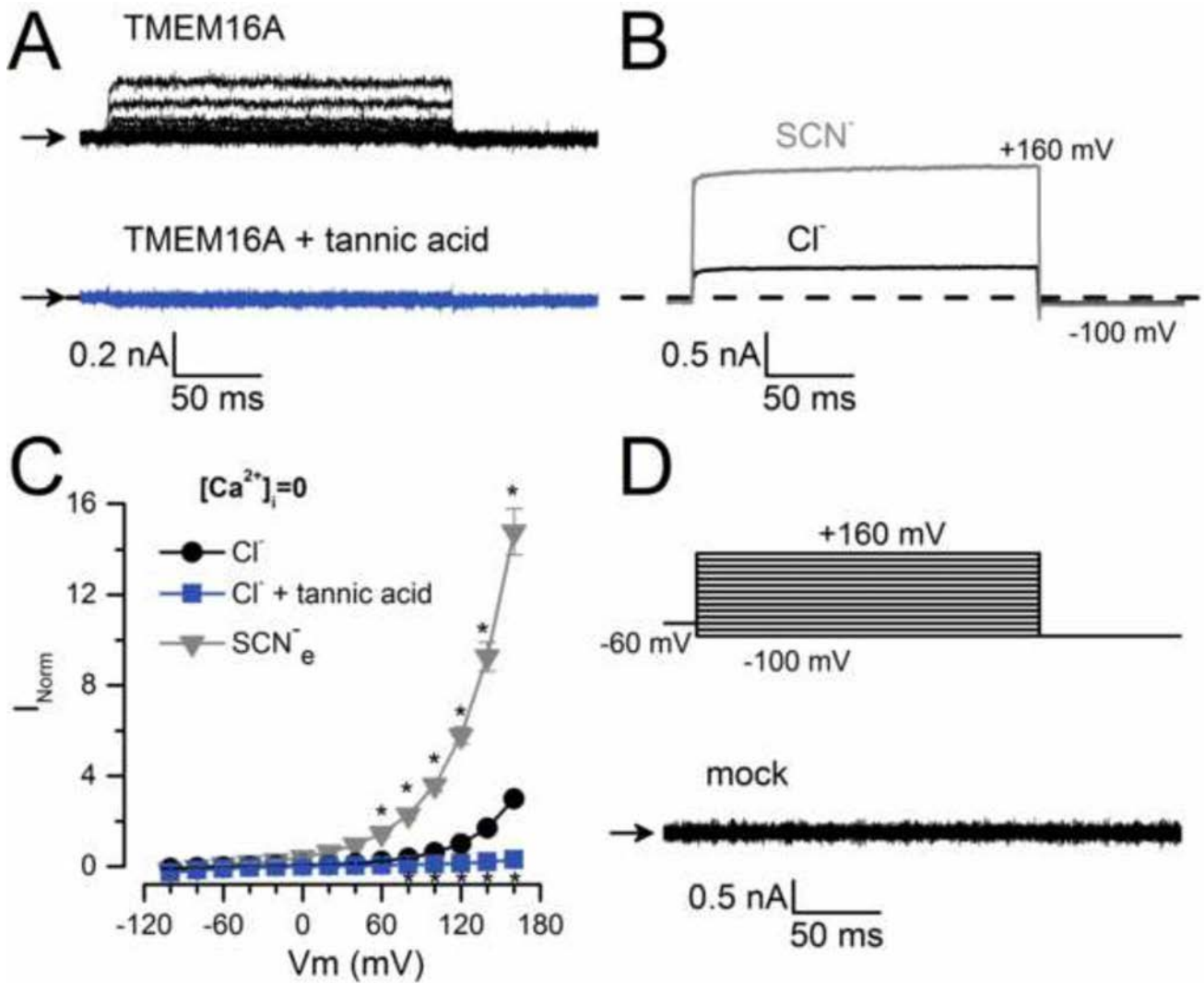


**Fig. 1. Activation of TMEM16A in zero intracellular Ca<sup>2+</sup>**

(A) Representative I<sub>Cl</sub> recordings (n=5) obtained from HEK293 cells expressing TMEM16A, bathed in a solution containing 0 (black traces) or 100 μM tannic acid (grey traces). (B) Representative current traces (n=5) obtained from the same cell bathed in 140 mM Cl<sup>-</sup> (black) or 140 mM SCN<sup>-</sup> (grey). Currents evoked by pulses to +160 mV followed by repolarization to -100 mV. (C) I<sub>Cl</sub>-V<sub>m</sub> relationships from cells bathed in [Cl<sup>-</sup>]<sub>o</sub>=140 mM (circles), [Cl<sup>-</sup>]<sub>o</sub>=140 mM + 100 μM of tannic acid (squares), or 140 mM SCN<sup>-</sup> (triangles). For each cell, whole cell currents were normalized to the current magnitude recorded at +120 mV from control cells bathed in [Cl<sup>-</sup>]<sub>o</sub>=140 mM. Normalized currents from different cells were averaged and plotted. (D) Lack of I<sub>Cl</sub> (n=6) in mock transfected cells dialyzed with a solution containing 40 mM [Cl<sup>-</sup>]<sub>i</sub>. In A and D the [Cl<sup>-</sup>]<sub>o</sub> was 140 mM and the I<sub>Cl</sub> were generated using the protocol shown in D. In all experiments, cells were dialyzed with 0 μM [Ca<sup>2+</sup>]<sub>i</sub> + 40 mM [Cl<sup>-</sup>]<sub>i</sub> (IS-40Cl/0Ca).

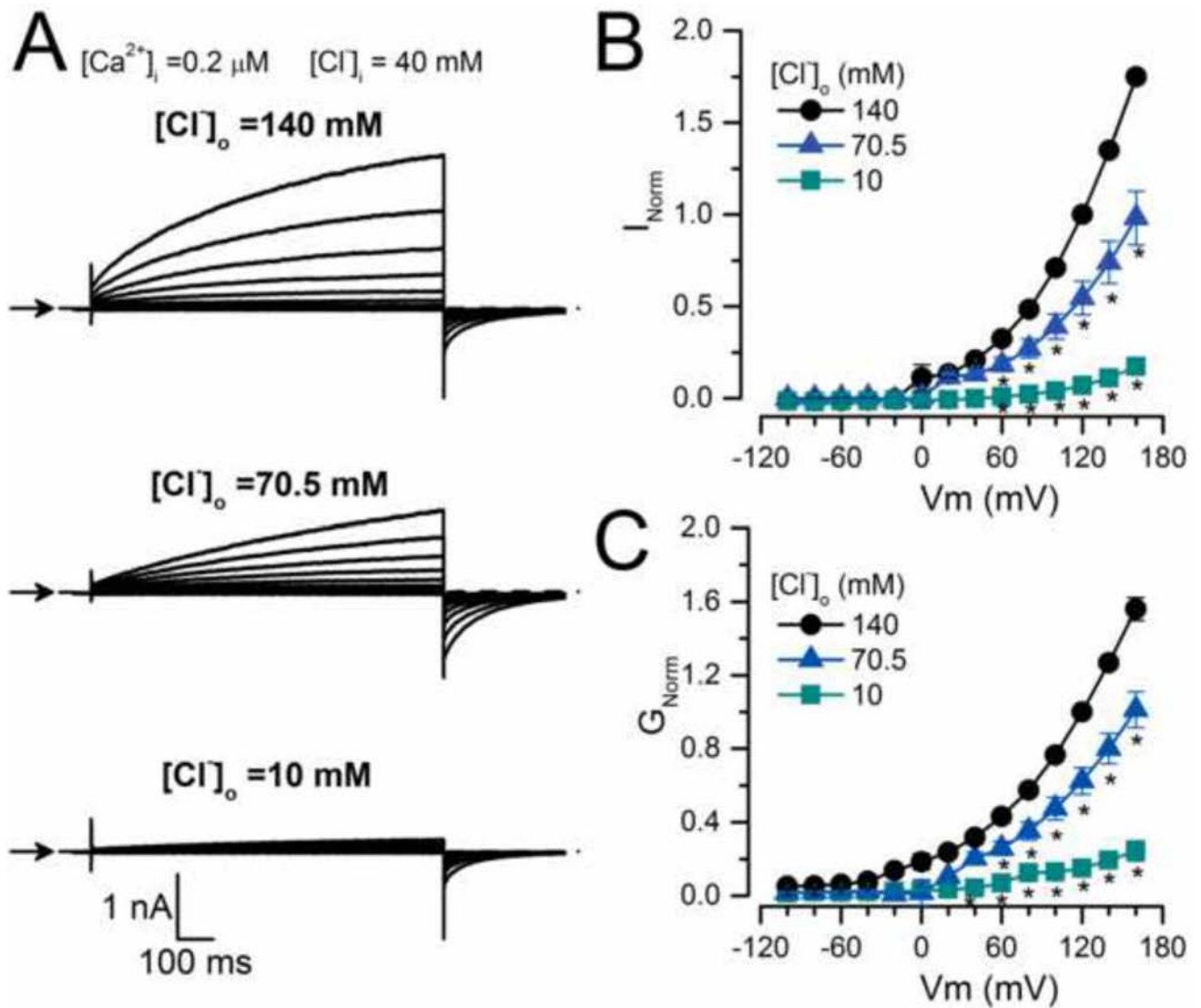


**Fig. 2. TMEM16A chloride conductance depends on  $[Cl^-]_o$**

(A) Representative  $I_{Cl}$  recordings ( $n=7$ ) obtained from the same cell sequentially bathed in ES containing 140, 70.5 and 10 mM  $[Cl^-]_o$  and dialyzed with an IS containing  $0.2 \mu M$   $[Ca^{2+}]_i$  + 40 mM  $[Cl^-]_i$  (IS-40.5Cl/0.2Ca). Cells were held at  $-60$  mV, then stepped for  $0.5$  s to voltages ranging from  $-100$  mV to  $+160$  mV in  $20$  mV increments and repolarised to  $-100$  mV. Note that  $I_{tail}$  at  $-100$  mV did not increase despite the increased driving force for  $Cl^-$  (i.e. driving force =  $-92.6 \pm 2.5$  mV with  $[Cl^-]_o$  140 mM and  $-146.2 \pm 4.6$  mV with 10 mM  $[Cl^-]_o$ ). (B)  $I_{Cl}$  vs  $V_m$  relationships at the indicated  $[Cl^-]_o$ . (C)  $G_{Norm}$  vs  $V_m$  curves at the indicated  $[Cl^-]_o$ .  $I_{Cl}$  and  $G$  were normalized to either  $I_{Cl}$  or  $G$  obtained at  $+120$  mV with  $[Cl^-]_o=140$  mM. External solutions with different  $[Cl^-]_o$  were prepared by mixing ES-136Cl and ES-1.5Cl.

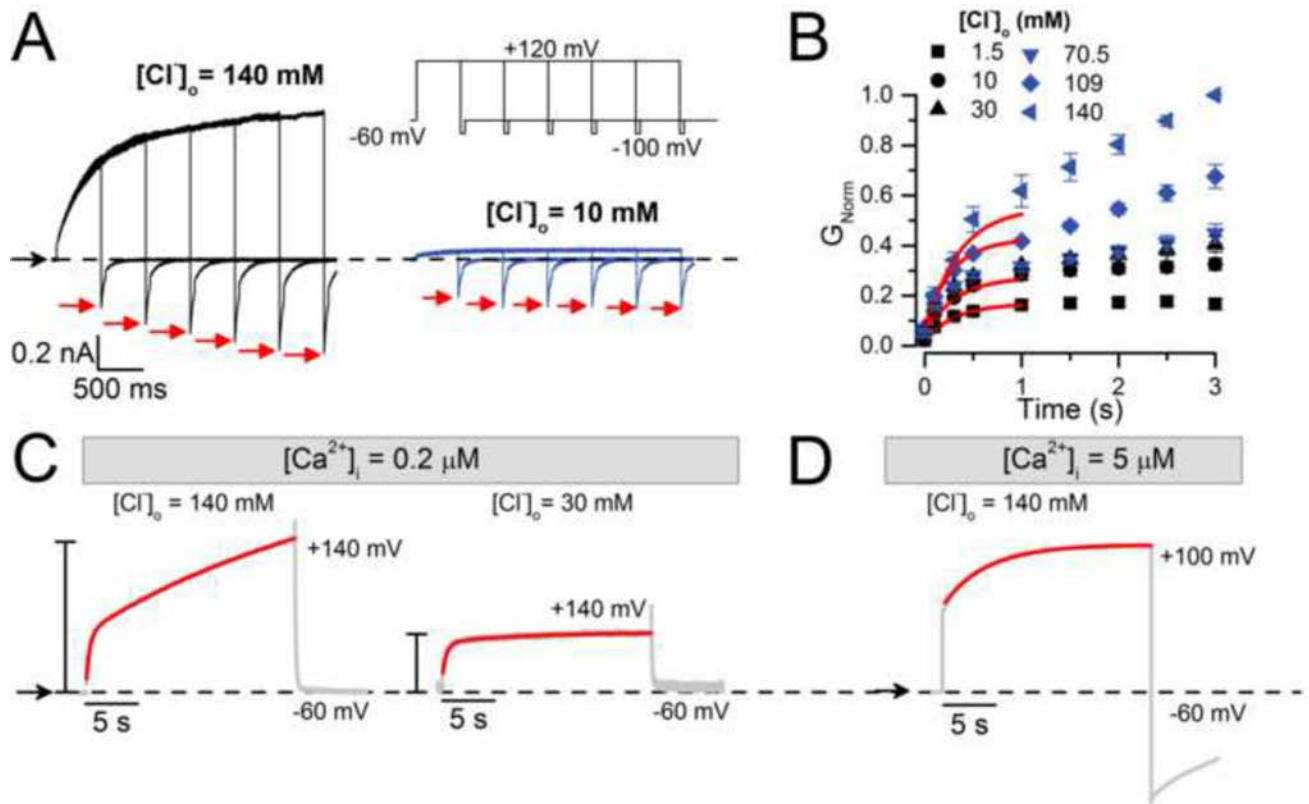


**Fig 3. Extracellular  $Cl^-$  regulates TMEM16A gating**

(A)  $I_{Cl}$  recordings from the same cell bathed in 140 mM (left) or 10 mM  $[Cl^-]_o$  (right).  $I_{Cl}$  was recorded using the  $V_m$  protocol shown in the inset. The duration of the test pulse increased from 0 to 3 s in 0.5 s steps. Arrows indicate the peak current amplitudes at -100 mV. (B) The magnitude of  $I_{tail}$  recorded as in A was used to determine the conductance at each time and  $[Cl^-]_o$  ( $n=5$ ).  $G_{Norm}$  was calculated using the  $G$  obtained with  $[Cl^-]_o=140$  mM and a 3s depolarization. Note that a single exponential can not describe the entire time course (continuous lines) when  $[Cl^-]_o = 30$  mM. (C)  $G_{Norm}(t)$  plots obtained from a cell stimulated with a 20 s depolarization to +140 mV and dialyzed with 0.2  $\mu M$   $Ca^{2+}_i$  (IS-40.5Cl/0.2Ca). The cell was exposed to 140 mM (left, ES-140Cl) and then to 30 mM (right, ES-30Cl)  $[Cl^-]_o$ .  $I_{Cl}$  was converted to  $G(t)$  and then normalized using the  $G$  value at +140 mV to determine  $G_{Norm}(t)$  at each  $[Cl^-]_o$  ( $n=4-8$ ).  $G_{Norm}(t)$  plots were fit with a bi-exponential function (continuous lines) to obtain  $\tau_s$ ,  $\tau_f$  and fractional contribution of each component. Note that the y-scale bar is 1 and 0.1 for 140 and 30 mM  $Cl^-$ , respectively. (D) TMEM16A- $I_{Cl}$  recorded from cells dialyzed with 5  $\mu M$   $[Ca^{2+}]_i$  (IS-40Cl/5Ca) and depolarized to +100 mV.  $I_{Cl}$  from each cell was normalized to  $I_{Cl}$  obtained with a 20 s depolarization and then normalized values were averaged ( $n=8$ ). The continuous line is the fit to a mono-exponential function.

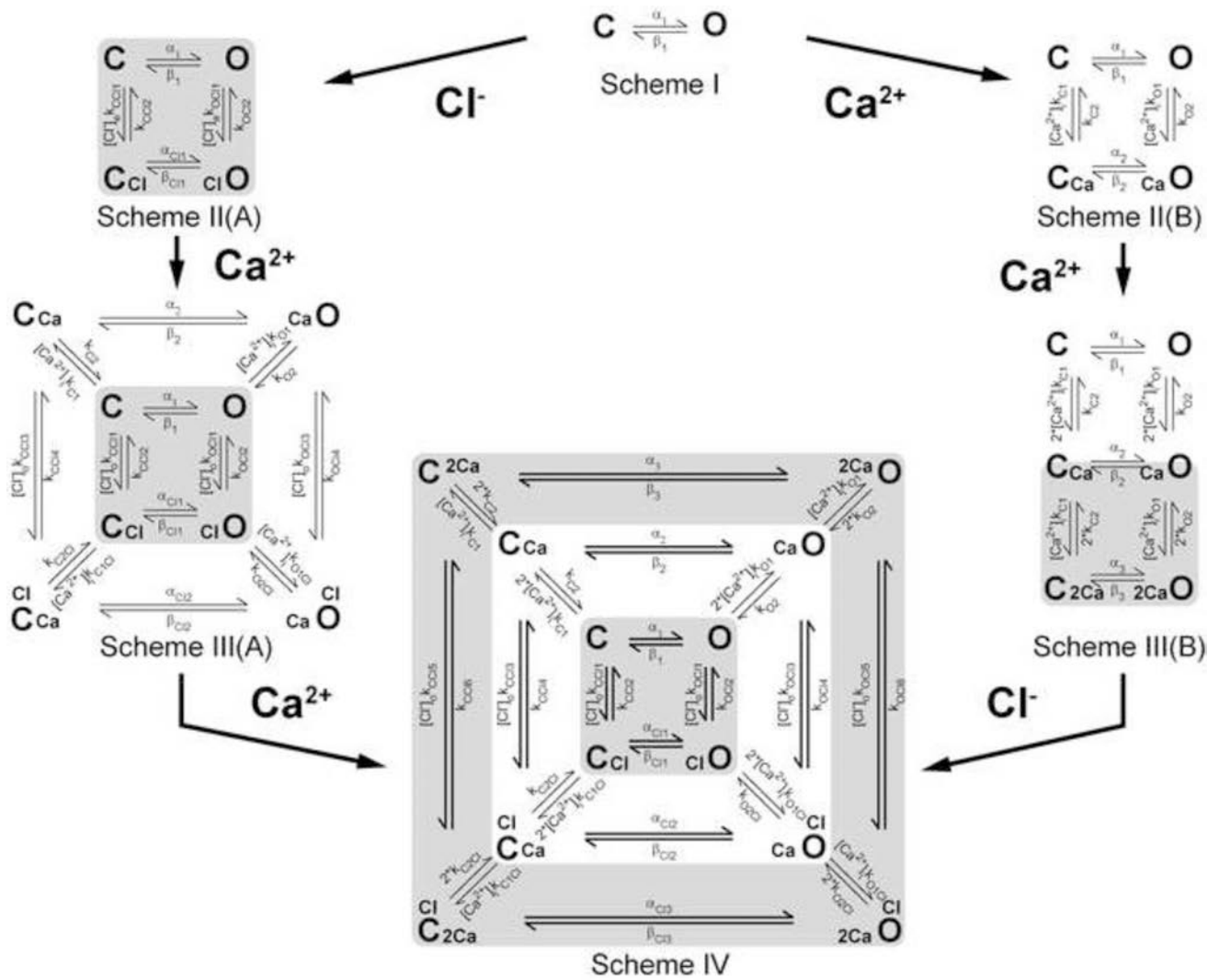


**Fig 4. Kinetic model employed to explain the  $V_m$ ,  $\text{Ca}^{2+}$ , and  $\text{Cl}^-$  contributions to TMEM16A gating**

**Scheme I** represents  $V_m$ -dependent transitions in the absence of intracellular  $\text{Ca}^{2+}$  and external  $\text{Cl}^-$ . C and O are closed and open states, and  $\alpha_1$  and  $\beta_1$  are  $V_m$ -dependent rate constants. **Scheme II(A)** represents the transitions in the presence of one external  $\text{Cl}^-$  when  $[Ca^{2+}]_i = 0$ .  $[Cl^-]_o k_{CC1}$  and  $[Cl^-]_o k_{OC1}$  are rate constants controlling  $\text{Cl}^-$  association to C and O configurations, while  $k_{CC2}$ ,  $k_{OC2}$  rate constants control  $\text{Cl}^-$  dissociation. **Scheme III(A)** results after binding of one  $\text{Ca}^{2+}$  to states represented in **Scheme II(A)**. The  $[Ca^{2+}]_i k_{O1}$ ,  $[Ca^{2+}]_i k_{O1Cl}$ ,  $[Ca^{2+}]_i k_{C1Cl}$  and  $[Ca^{2+}]_i k_{C1}$  are  $\text{Ca}^{2+}$  association rate constants while  $k_{O2}$ ,  $k_{O2Cl}$ ,  $k_{C2Cl}$  and  $k_{C1}$  are  $\text{Ca}^{2+}$  dissociation rate constants. The subscript Cl indicates rate constants associated with  $\text{Cl}^-$ -occupied transitions. **Scheme II(B)** represents transitions resulting after binding of one intracellular  $\text{Ca}^{2+}$  to C and O states depicted in **Scheme I**.  $[Ca^{2+}]_i k_{C1}$ ,  $[Ca^{2+}]_i k_{O1}$  are rate constants controlling  $\text{Ca}^{2+}$  association to C and O configurations, while  $k_{C2}$ ,  $k_{O2}$  rate constants control  $\text{Ca}^{2+}$  dissociation. **Scheme III(B)** represents the transitions resulting after binding of an additional  $\text{Ca}^{2+}$  to states shown in **Scheme II(B)**. Association and dissociation of the second  $\text{Ca}^{2+}$  was assumed to be same as

for the first  $\text{Ca}^{2+}$  binding reaction. **Scheme IV** results after binding of an additional  $\text{Ca}^{2+}$  to states shown in **Scheme III(A)**. The association and dissociation rate constants were the same as that for the first  $\text{Ca}^{2+}$  binding (left pathway). Alternatively, **Scheme IV** could be achieved after binding of one external  $\text{Cl}^-$  to states shown in **Scheme III(B)** with forward rate constants  $[\text{Cl}^-]_o k_{\text{CC15}}$ ,  $[\text{Cl}^-]_o k_{\text{CC13}}$ ,  $[\text{Cl}^-]_o k_{\text{CC11}}$ ,  $[\text{Cl}^-]_o k_{\text{OC11}}$ ,  $[\text{Cl}^-]_o k_{\text{OC13}}$  and  $[\text{Cl}^-]_o k_{\text{OC15}}$  and backward rate constants  $k_{\text{CC16}}$ ,  $k_{\text{CC14}}$ ,  $k_{\text{CC12}}$ ,  $k_{\text{OC12}}$ ,  $k_{\text{OC14}}$  and  $k_{\text{OC16}}$ . Concentric kinetic cycles with states connected by wider arrows indicate cycles that did not satisfy microscopic reversibility. Table 2A shows the Equations for each rate constant.

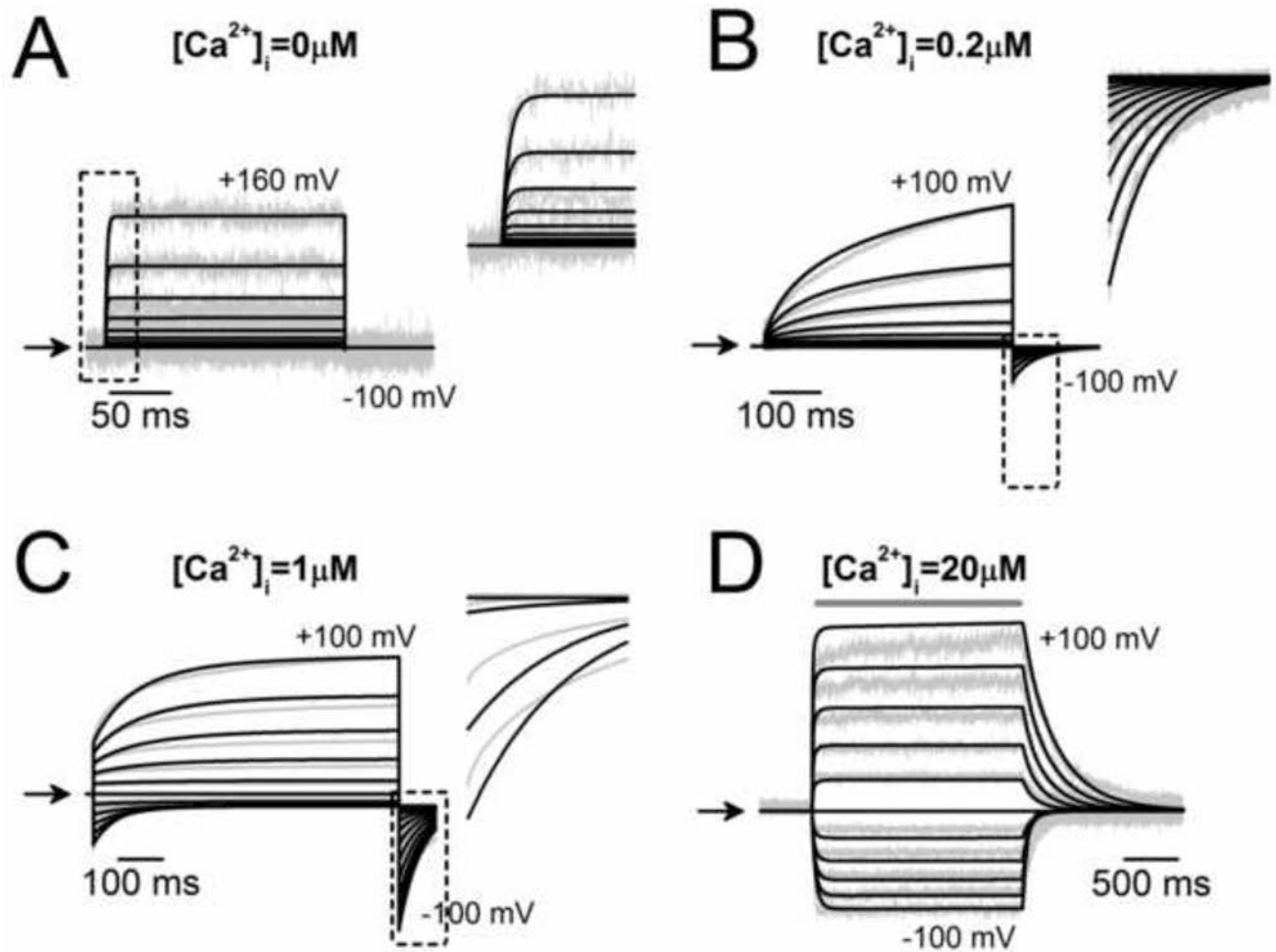


**Fig 5.** Global fit using Scheme IV to TMEM16A recordings obtained at different  $V_m$  and  $[Ca^{2+}]_i$ . Best fits were performed with the IChMASCOT software; solid lines are fits and grey lines are data. **(A–C)** Fits to  $I_{Cl}$  recordings obtained between  $-100$  mV to  $+100$  mV ( $20$  mV increments) from cells dialyzed with  $0$  (A),  $0.2$  (B), or  $1$  (C)  $\mu M$   $[Ca^{2+}]_i$ . **D** Best fits to data obtained by fast perfusion with  $20$   $\mu M$   $[Ca^{2+}]_i$  to an inside-out patch held at  $V_m$  between  $-100$  mV to  $+100$  mV. The insets in A, B and C show magnified fits to fast phases of  $I_{Cl}$  enclosed in black squares.  $I_{Cl}$  shown in **A** and **B** were recorded from cells dialyzed with  $[Cl^-]_i = 40$  mM; C and **D** were from cells exposed to symmetrical  $140$  mM  $Cl^-$ .



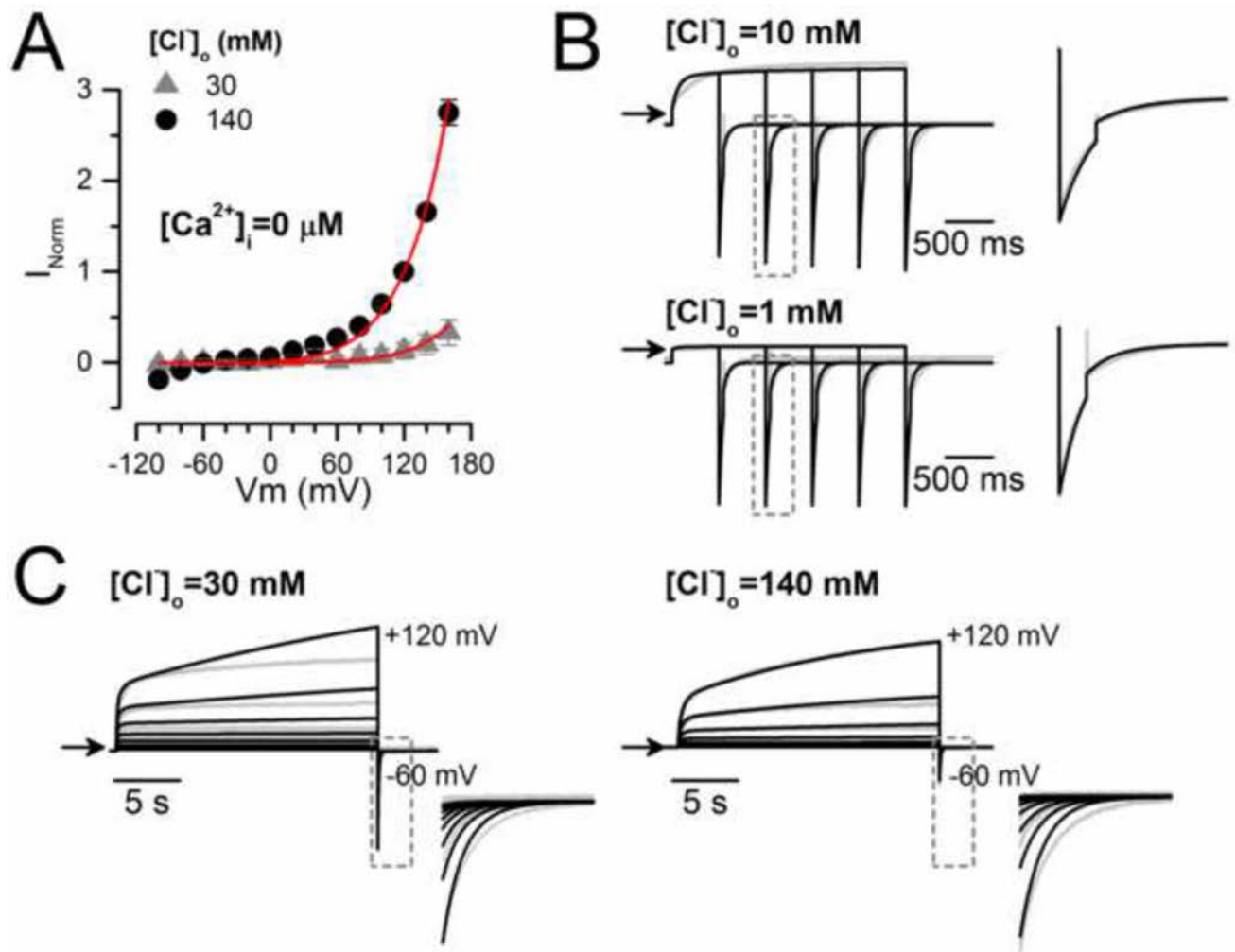


**Fig 6. Global fit using Scheme IV to TMEM16A recordings obtained at different  $[Cl^-]_o$**   
 Grey lines are data and solid lines are best fits to: (A)  $I-V_m$  relationships obtained with 30 mM and 140 mM  $[Cl^-]_o$  from cells dialyzed with a zero  $Ca^{2+}$  solution; (B)  $I_{Cl}$  recorded from the same cell exposed to 10 mM and 1 mM  $[Cl^-]_o$ , dialyzed with 0.2  $\mu M$   $[Ca^{2+}]_i$  and stimulated with the  $V_m$  protocol shown in Figure 3A; (C)  $I_{Cl}$  recorded from cells exposed to 30 mM and 140 mM  $[Cl^-]_o$ , dialyzed with 0.2  $\mu M$   $[Ca^{2+}]_i$  and stimulated with 20 s pulses from  $-20$  mV to  $+120$  mV. Data in B and C were obtained from cells dialyzed with  $[Cl^-]_i = 40$  mM. The right insets in B and C show magnified fits to fast phases of  $I_{tail}$  enclosed in grey squares. The  $R^2$  value for the global fits shown in Figures 5 and 6 was 0.98.

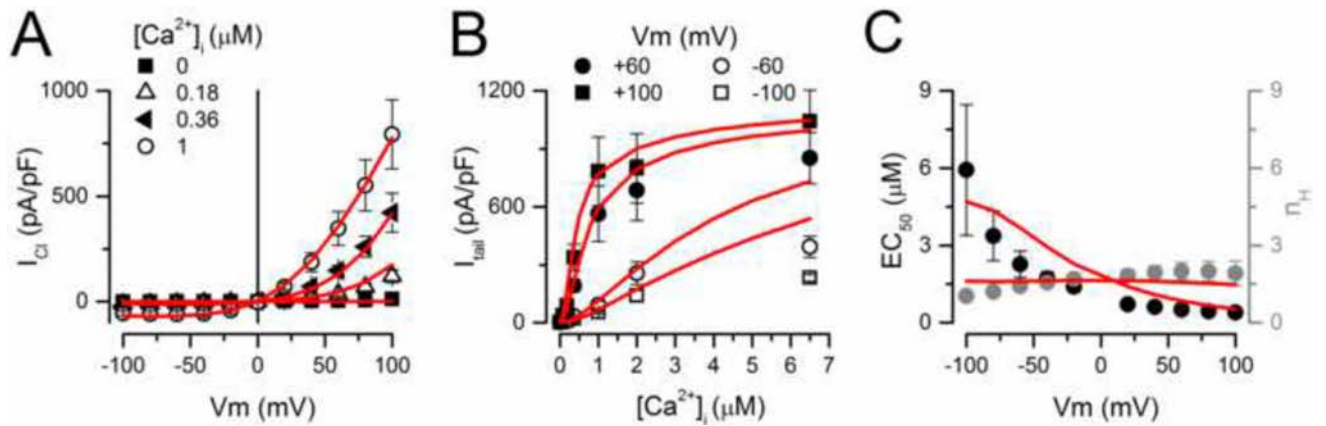


**Fig 7. Scheme IV mimics the  $I_{Cl}$  vs  $V_m$ , dose-response curve to  $[Ca^{2+}]_i$  and the  $EC_{50}/n_H$  vs  $V_m$  relationships for TMEM16A channels**

Black symbols correspond to experimental data. Solid lines are simulations using Scheme IV. (A) Current Density vs  $V_m$  relationships. (B) Current Density as a function of  $[Ca^{2+}]_i$  at the indicated  $V_m$ . (C)  $EC_{50}$  for TMEM16A  $Ca^{2+}$  activation and the Hill coefficient  $n_H$  vs  $V_m$ .  $EC_{50}$  and  $n_H$  values were obtained from B. The experimental data was collected using  $[Cl^-]_i=[Cl^-]_o=140$  mM and 0.7 s depolarizations. The same conditions were used in the simulations. All simulations were carried out using the IonChannelLab software and the rate constants listed in Table 2.  $R^2 = 0.95$ .

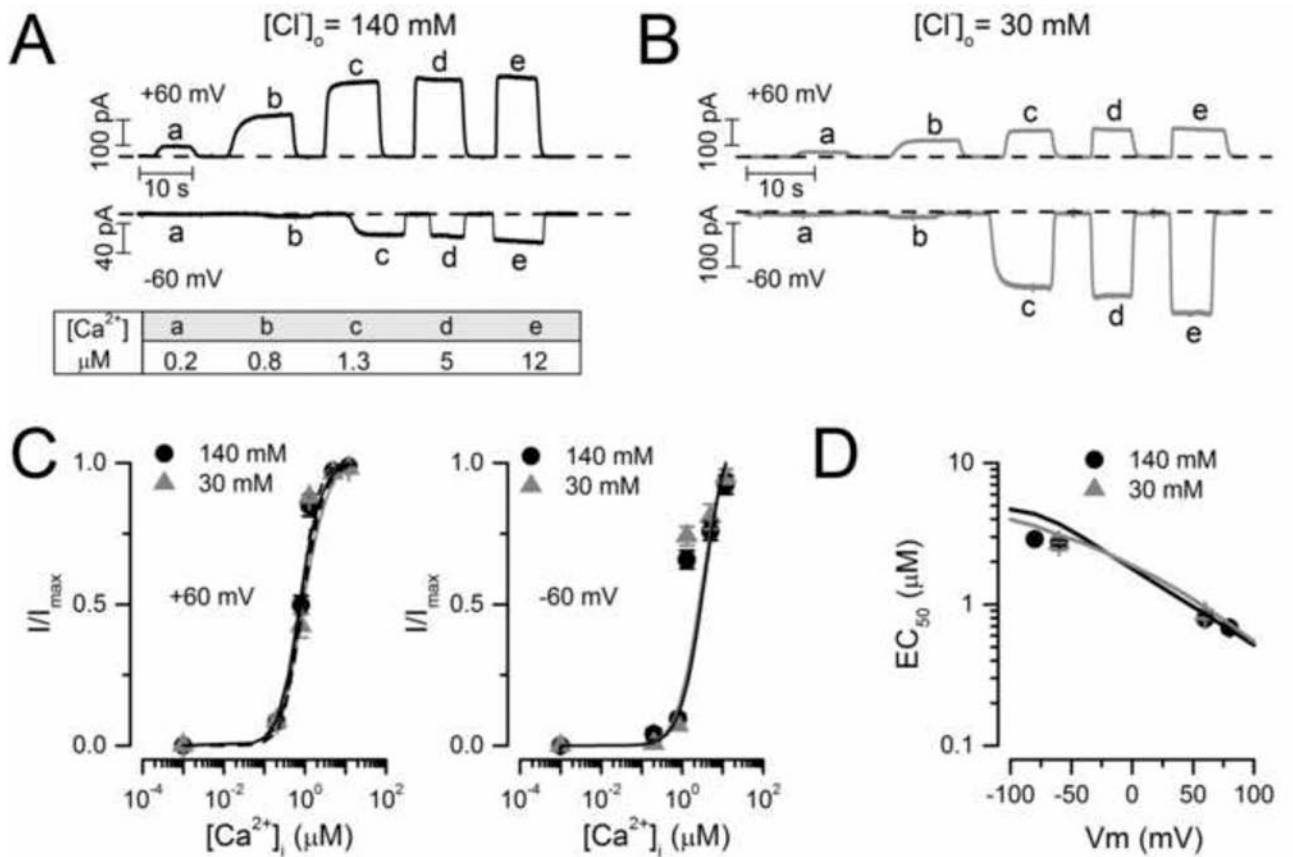


**Fig 8. The apparent  $Ca^{2+}$  sensitivity of TMEM16A was not altered by lowering the  $[Cl^-]_o$**   
**A–B** Typical  $I_{Cl}$  recordings from inside-out patches held at  $\pm 60$  mV and exposed to 140 mM **(A)** or 30 mM  $[Cl^-]_o$  **(B)**.  $I_{Cl}$  were activated by applying 0, 0.2 **(a)**, 0.8 **(b)**, 1.3 **(c)**, 5 **(d)** and 12  $\mu\text{M}$   $[Ca^{2+}]_i$  **(e)**. Dashed lines indicate  $I_{Cl}$  obtained with 0  $[Ca^{2+}]_i$  and 25.2 mM EGTA. **(C–D)** Dose-response and  $EC_{50}$  vs  $V_m$  curves (symbols) obtained from experimental data like that shown in **A and B** were identical to the predictions made with Scheme IV at 30 (grey lines) and 140 (black lines) mM  $[Cl^-]_o$ .

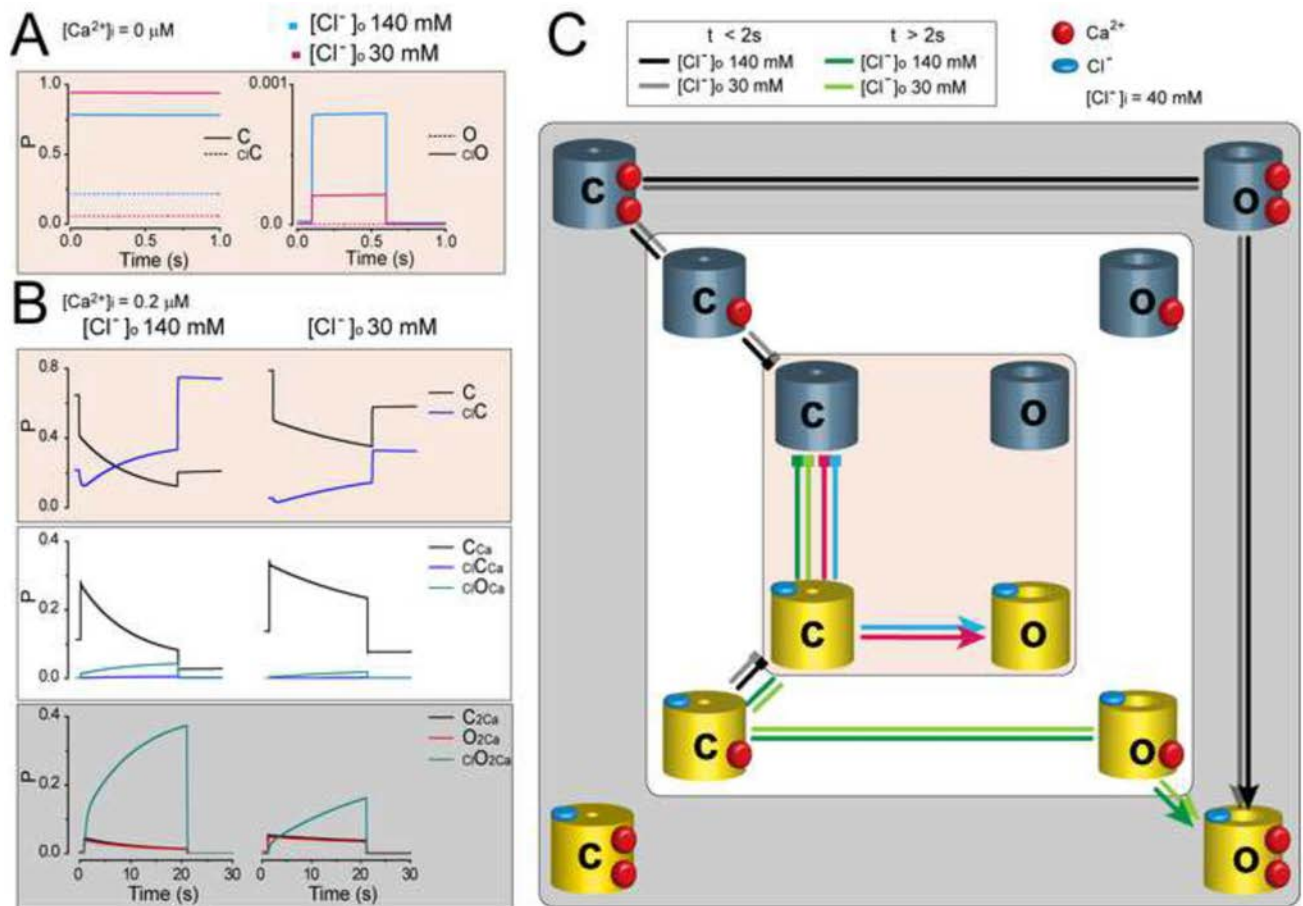


**Fig 9. TMEM16A activation pathways predicted by Scheme IV**

(A) Time dependent  $P_C$ ,  $P_O$ ,  $P_{cC}$  and  $P_{cO}$  when  $[Cl^-]_o$  was 140 mM (blue lines) or 30 mM (red lines) while  $[Ca^{2+}]_i$  and  $[Cl^-]_i$  were 0 M and 40 mM, respectively. Note that  $P_O$  was  $\approx 0$  at both  $[Cl^-]$ . (B) Time dependent  $P_C$ ,  $P_{cC}$ ,  $P_{cCa}$ ,  $P_{cClCa}$ ,  $P_{cClOca}$ ,  $P_{cOca}$ ,  $P_{cO2Ca}$ , and  $P_{cClO2Ca}$  are shown in rectangles coloured according to the colours of the layers of Scheme IV presented in panel C. Left column:  $[Ca^{2+}]_i = 0.2 \mu M$ ,  $[Cl^-]_o/[Cl^-]_i = 140/40 mM$ . Right column:  $[Ca^{2+}]_i = 0.2 \mu M$ ,  $[Cl^-]_o/[Cl^-]_i = 30/40 mM$ .  $P_O$ ,  $P_{cO}$ ,  $P_{cOca}$ , and  $P_{cClcOca}$  are not shown for clarity, their values were  $\approx 0$ . P values were calculated by numerically integrating the differential equations (supplemental material) under the following conditions:  $[Cl^-]_o = 140 mM$  or  $30 mM$ ,  $[Cl^-]_i = 40 mM$ ,  $[Ca^{2+}]_i = 0$  (A),  $0.2$  (B)  $\mu M$ , and  $20 s$  pulse to  $+140 mV$  followed by repolarization to  $-60 mV$ . The set of rate constants listed in Table 2 was used to obtain the time dependence of occupation probability. (C) TMEM16A activation pathways according to probability of occupation. Blue and pink arrows indicate the pathway in the absence of intracellular  $Ca^{2+}$  while  $[Cl^-]_o$  was 140 mM or 30 mM, respectively. Black, grey, green and light green arrows indicate the activation pathways when intracellular  $Ca^{2+}$  was  $0.2 \mu M$  while  $[Cl^-]_o$  was 140 mM (black and green lines) or 30 mM (grey and light green lines).  $[Cl^-]_i$  was set at 40 mM. Red button =  $Ca^{2+}$ , blue donut =  $Cl^-$ .

**Recording solutions**

**Table 1**

External solutions with different [Cl<sup>-</sup>] were prepared by mixing solutions ES-136Cl<sup>-</sup>, ES-10Cl<sup>-</sup> and ES-1.5Cl<sup>-</sup> to obtain the required Cl<sup>-</sup> concentration.

Compound	External solutions (mM)				
	ES-140Cl	ES-140Na	ES-10Cl	ES-1.5Cl	ES-30Cl
TEA-Cl	139	-	9	0.5	29
NaCl		139	-	-	
CaCl <sub>2</sub>	0.5	0.5	0.5	0.5	0.5
HEPES	20	20	20	20	20
D-Mannitol	100	100	300	320	330
Osmolarity (mosm/kg)	390	390	340	340	390
Total [Cl <sup>-</sup> ]	140	140	10	1.5	30

Compound	Internal solutions (mM)						
	IS-40Cl/0Ca	IS-40Cl/0.2Ca	IS-40Cl/0.8Ca	IS-40Cl/1.3Ca	IS-40Cl/5Ca	IS-40Cl/12Ca	IS-83Cl/0.2Ca
TEA-Cl	40	30	17	27.4	11.8	2	72.5
CaCl <sub>2</sub>	-	5.2	11.5	6.3	14.1	19	5.2
HEPES	50	50	50	50	50	50	50
D-Mannitol	90.2	85	150	154	85	85	-
EGTA-TEA	25.2	25.2	25	-	-	-	25.2
HEDTA	-	-	-	25	25	25	-
Osmolarity (mosm/kg)	290	290	290	290	290	290	288
Free [Ca <sup>2+</sup> ] (μM)	0	0.2	0.8	1.3	5	12	0.2
Total [Cl <sup>-</sup> ]	40	40	40	40	40	40	83

**Table 2**  
**Parameter values associated with the rate constants of Scheme IV**

(A) Figures listed were obtained from the global fit of TMEM16A data shown in Figures 5 and 6.  $z$  values are the apparent charge. (B) The relationship between forward and backward rate constants and weight factors  $l$ ,  $L$ ,  $h$ ,  $H$ ,  $m$  and  $M$ —which take into account the presence of  $\text{Ca}^{2+}$  in a given state. Grey boxes include weight factor values obtained from the global fit. Values shown in *Italics* and parenthesis (A and B) are averaged values obtained during the first 15 fit trials and were used as a seed for the final global fit. All listed parameter values were used for simulations of Scheme IV shown in Figures 7, 8 and 9.

<b>A</b>			
Rate Constant	Expression	Parameter	Parameter Values At 0 mV
$\alpha_1$	$\alpha_{1,0} e^{\frac{z_{\alpha} FV_m}{RT}}$	$\alpha_{1,0} (s^{-1})$	0.0077 (0.00803±0.00064)
		$z_{\alpha}$	0 (0±0)
$\beta_1$	$\beta_{1,0} e^{\frac{-z_{\beta} FV_m}{RT}}$	$\beta_{1,0} (s^{-1})$	917.1288 (875.07±51.77)
		$z_{\beta}$	0.0064 (0.01133±0.0021)
$k_{O1}$	$k_{O1,0} e^{\frac{z_1 FV_m}{RT}}$	$k_{O1,0} (s^{-1} \mu M^{-1})$	597.9439 (583.58±14.41)
		$z_1$	0 (0±0)
$k_{O2}$	$k_{O2,0} e^{\frac{-z_2 FV_m}{RT}}$	$k_{O2,0} (s^{-1})$	2.8530 (2.8547±0.0189)
		$z_2$	0.1684 (0.166±0.00118)
$\alpha_{CI}$	$k_{1,0} e^{\frac{z_{11} FV_m}{RT}}$	$k_{1,0} (s^{-1})$	1.8872 (1.9349±0.0708)
		$z_{11}$	0.1111 (0.1141±0.00403)
$\beta_{CI}$	$k_{2,0} e^{\frac{-z_{12} FV_m}{RT}}$	$k_{2,0} (s^{-1})$	5955.783 (5769.96±207.83)
		$z_{12}$	0.3291 (0.3272±0.00346)
$k_{CC1}$	$k_{+Cl,0} e^{\frac{z_{+Cl} FV_m}{RT}}$	$k_{+Cl,0} (s^{-1} mM^{-1})$	1.143×10 <sup>-6</sup> (1.14×10 <sup>-6</sup> ±9.17×10 <sup>-8</sup> )
		$z_{+Cl}$	0.1986 (0.2112±0.0238)
$k_{CC2}$	$k_{-Cl,0} e^{\frac{-z_{-Cl} FV_m}{RT}}$	$k_{-Cl,0} (s^{-1})$	0.0009 (8.52×10 <sup>-4</sup> ±1.28×10 <sup>-5</sup> )
		$z_{-Cl,0}$	0.0427 (0.04847±0.0098)
$k_{OC1}$	$k_{+O1,0} e^{\frac{z_{+O1} FV_m}{RT}}$	$k_{+O1,0} (s^{-1} mM^{-1})$	1.1947 (1.1495±0.0459)
		$z_{+O1}$	0.6485 (0.65±0.0026)
$k_{OC2}$	$k_{-O1,0} e^{\frac{-z_{-O1} FV_m}{RT}}$	$k_{-O1,0}$	3.4987 (3.443±0.1096)
		$z_{-O1}$	0.0300 (0.0308±0.00054)
<b>B</b>			
$\alpha_2 = l\alpha_1$	$\alpha_3 = l^2\alpha_1$	$\beta_2 = L\beta_1$	$\beta_3 = L^2\beta_1$
$k_{CCB} = hk_{CC1}$	$k_{CCB} = h^2k_{CC1}$	$k_{CC4} = Hk_{CC2}$	$k_{CC6} = H^2k_{CC2}$
$k_{OCB} = mk_{OC1}$	$k_{OCB} = m^2k_{OC1}$	$k_{OC4} = Mk_{OC2}$	$k_{OC6} = M^2k_{OC2}$
$k_{C1C1} = \frac{h}{H}k_{O1}$	$k_{C2C1} = \frac{l}{L}k_{O2}$	$k_{O1C1} = \frac{m}{M}k_{O1}$	$k_{O2C1} = k_{O2}$

$\alpha_{C12} = \frac{Hml}{M} \alpha_{C11}$	$\alpha_{C13} = \frac{Hml^2}{M^2} \alpha_{C11}$	$\beta_{C2} = hL\beta_{C1}$		$\beta_{C3} = (hL)^2\beta_{C1}$
$k_{C1} = k_{O1}$	$k_{C2} = \frac{l}{L} k_{O2}$	$l = 41.6411 (42.04 \pm 1.7)$	$m = 0.0102 (0.010 \pm 0.00023)$	$h = 0.3367 (0.342 \pm 0.018)$
		$L = 0.1284 (0.134 \pm 0.004)$	$M = 0.0632 (0.064 \pm 0.001)$	$H = 14.2956 (14.2 \pm 0.70)$

Author Manuscript

Author Manuscript

Author Manuscript

Author Manuscript